Departament de Teoria del Senyal i Comunicacions
UNIVERSITAT POLITÈCNICA DE CATALUNYA

Master Thesis

GROUND-BASED SAR IMAGING BASICS AND LAND CLUTTER EFFECTS IN THE FOCUSED IMAGE

Marc Lort Cuenca

Albert Aguasca Solé, Master Thesis Advisor

Barcelona, September 2014

A mi compañera de viaje,

Irina Chic, por ayudarme a respirar cuando no había oxígeno

A los "Intocables", que son y serán

A mi compañero,

Israel Durán, por visualizar lo que hoy es

A mi madre,

Roser Lort Cuenca, porque sin ella nada de esto sería posible…

Contents

Introduction

Remote Sensing is the science and art of obtaining information about an object, area, or phenomenon through the analysis of data acquired by a device that is not in contact with the object, area, or phenomenon under investigation. The different remote sensing technologies can be widely classified in two categories; passive remote sensing and active remote sensing. Remote sensing systems which measure energy that is naturally available are called passive sensors. Passive sensors can only be used to detect energy when the naturally occurring energy is available. Reflected sunlight is the most common source of radiation measured by passive sensors. Examples of passive remote sensors include filmphotography, infrared, charge-coupled devices, and radiometers. Active sensors, on the other hand, provide their own energy source for illumination. The sensor emits radiation which is emitted towards the target to be investigated. The radiation reflected from that target is detected and measured by the sensor. An important example of active remote sensing sensor is the *Synthetic Aperture Radar* (SAR).

SAR is a form of radar whose defining characteristic is the use of the relative motion between its antenna and the target region to provide distinctive long-term coherent signal variations that are exploited to obtain finer spatial resolution than is possible with conventional beam-scanning means. SAR is typically mounted on a moving platform such as an aircraft or spacecraft. The distance the SAR device travels over a target creates a large "synthetic" antenna aperture. The basic idea of the SAR is that the larger the aperture is, the higher the image resolution becomes. This allows SAR to create high resolution images with comparatively small physical antennas.

In spite of the fact that the use of satellite-borne systems is extremely successful for the study of the evolution of slow-time processes over wide areas, it reveals being often unsuitable when high flexibility in terms of revisiting time is needed, as to foresee possible hazard conditions. For this reason, during the last years the research activity of several remote sensing groups has been devoted to the development of terrestrial SAR systems. Easy to deploy, extremely cheaper if compared to space-borne solutions, *ground-based SAR* (GBSAR) sensors represent a cost-effective solution for the continuous monitoring of small scale phenomena. These systems basically consist of a *continuous wave* (CW) radar mounted on a sliding support and synthesizing in time an aperture longer than the physical dimension of their real antennas. The aim is to merge the SAR capability to obtain 2D reflectivity images and the advantages offered by a terrestrial platform, such as the high stability, the perfect knowledge of sensor's track and the absence of any revisiting time constrain.

The organization of the Master Thesis is consequently as follows:

In **Chapter 2,** the basic principles of radar imaging will be recalled, such as the range direction and the cross-range direction or the radar swath. Some formulation for the radar resolution, the *Signal to Noise Ratio* (SNR) or the radar equation will be derived. Differences between real aperture radars and synthetic aperture radars will be addressed. To comprise the basis of operation of the synthetic aperture radar, the range domain and the cross-range domain description will be studied in detail.

In **Chapter 3,** the effect of an oscillating target in the focused image will be analyzed. With this purpose, some simulations and measurements will be performed. The X Band and the *Universitat Politècnica de Catalunya* (UPC) W Band GBSAR will be employed to analyze that effects and the results obtained will be contrasted with the previous simulations.

In **Chapter 4,** the windblown radar ground clutter will be studied. As the scintillation of the vegetation is an important phenomenon that has its impact in the focused image, some simulations and measurements will be performed to determine the nature of such effect. The measurements will be realized with the UPC X Band GBSAR over the Collserola range and the Montserrat test site. All the results obtained in the measurement campaigns will be contrasted with a simulated model for the Doppler spectrum of windblown radar ground clutter and the consistence of the results will be analyzed.

Finally, **Chapter 5** will summarize the obtained results and will expose the main conclusions coming out from this Master Thesis research study.

To conclude the present master thesis dissertation, the **Appendix A** has been incorporated. As many of the measurements exposed in the present work have been done with a system developed by the UPC *Remote Sensing Laboratory* (RSLab), the main characteristics of its architecture will be presented and its performance will be evaluated.

Synthetic Aperture Radar (SAR) Imaging Basics

Ap.1 Introduction to radar

The word “radar” is an acronym for “radio detection and ranging”. A radar determines the distance to an object by measuring the elapsed time between the echo reflected from that object and the transmitted electromagnetic signal. The total distance traveled by the signal is twice the distance between the radar and the object, since the signal travels from the radar to the object and the back from the object to the radar. Therefore, once the propagation time (t) is measured and taking into account that the signal propagates at the speed of light, the range (R)can be easily calculated as

$$R = \frac{1}{2}ct \qquad \textbf{Equation 2.1 - 1}$$

where c is the speed of light in the medium.

Radars are known as active, remote-sensing instruments that can be used not only during day or night but also under (almost) all weather conditions. Imaging remote-sensing radars, such as synthetic aperture radars (SAR), produce high resolution images of surfaces. The geophysical information can be derived from these images by using proper post processing techniques.

This chapter focuses on the basics of radar imaging and describes the synthetic aperture principle.

Ap.2 Basic Principles of Radar Imaging

There are two different mechanisms by which imaging radars can be used to produce images and, depending on the mechanism used, they can be broadly classified between real aperture and synthetic aperture radars. The differences between these two types of radar will be discussed in detail later in this chapter.

Radar images are typically acquired as the satellite or aircraft carrying the radar system moves along its flight path. To separate objects in the cross-track direction and the along-track direction within a radar image, two different methods must be implemented. The cross-track

direction, also known as the range direction, is the direction perpendicular to the one in which the imaging platform is moving. In this direction, radar echoes are separated using the time delay between the echoes. The along-track direction, also known as the azimuth direction or cross-range direction, is the direction parallel to the movement of the imaging platform. The angular size (in the case of real aperture radar) or the Doppler history (in the case of SAR) is used to separate surface pixels in this direction. Using the time delay in the range direction and Doppler history results in azimuth direction, SAR images have resolutions that are independent of the distance from the radar to the scene, as will be discussed later in the present chapter.

The imaging radar sensor uses an antenna with a certain beam width to illuminate the surface with a pulse of electromagnetic energy, as shown in Figure 2 - 1.

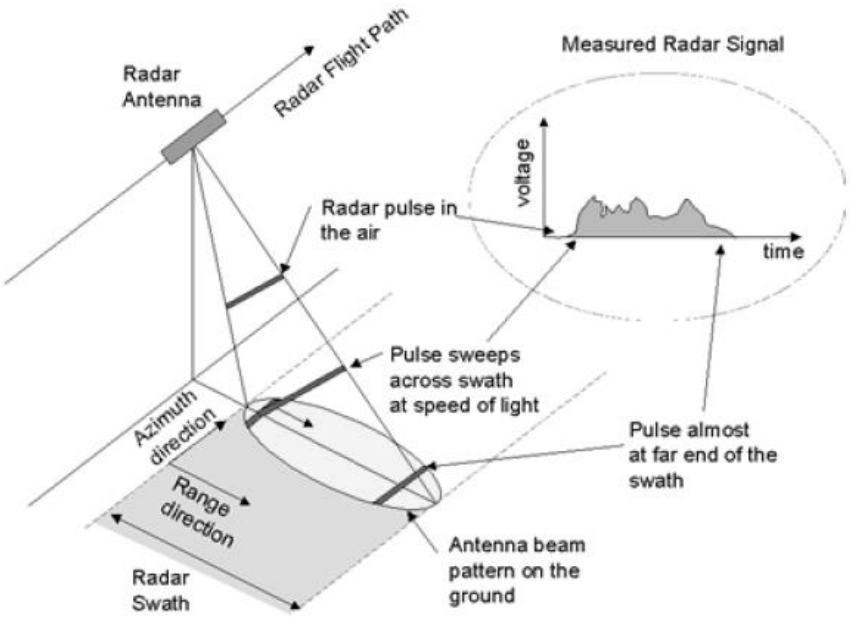

Figure 2 - 1 Imaging geometry for a side-looking radar system

Echoes from surface points that are located farther away along the azimuth direction will be received at proportionally later times, allowing to subdivide the surface into a series of range bins by dividing the receive time in increments of equal time bins. The antenna footprint along the track sets the width in the azimuth direction of each range bin. The sets of range bins are covered sequentially with the movement of the platform. The brightness associated to each image pixel in the radar image is proportional to the echo power of the corresponding time bin. As will be seen later, the difference between real aperture radars and synthetic aperture radars lies in how the azimuth resolution is achieved.

There are two different meanings for the term “range” in radar imaging, which are the slant range and the ground range (as shown in Figure 2 - 2).

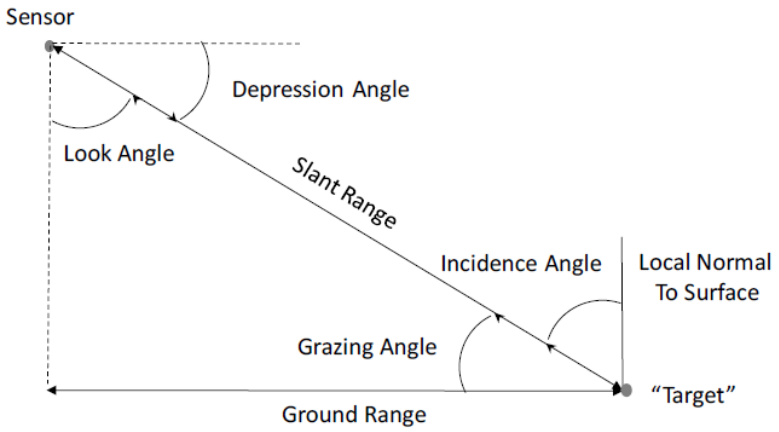

Figure 2 - 2 Definition of some common radar imaging terms

The slant range is measured between the radar and the scatterer and the ground range refers to the range between the position directly underneath the radar and the scatterer. In the Figure 2 - 2 are also defined the look angle, the incidence angle, the depression angle and the grazing angle. The look angle is defined as the angle between the vertical direction and the radar beam of the radar. The incidence angle is defined as the angle between the vertical direction and the radar wave propagation vector at the surface. The depression angle is the angle between the radar beam and the horizontal at the radar platform. Finally, the grazing angle is the angle between the horizontal in the surface and the incident wave.

Ap.3 Radar Resolution

The resolution of an image is defined as the capability to distinguish two closely spaced targets. Considering two targets in the slant range direction spaced by x_r, the corresponding echoes will be separated by a time difference Δt equal to:

$$\Delta t = \frac{2x_r}{c} \qquad \textbf{Equation 2.3 - 1}$$

where c is the speed of light and the factor 2 takes into account the distance traveled by the signal to the object and backwards to the radar. A radar usually transmits radar pulses. The two targets can be discriminated if the pulse returned by the second target is received later than the pulse received from the first target (no overlapping). Therefore, the smallest separable time difference in the radar receiver is equal to the effective time length τ of the pulse. Thus, the slant range resolution of a radar is:

$$\tau = \frac{2x_r}{c} \implies x_r = \frac{c\tau}{2} \qquad \textbf{Equation 2.3 - 2}$$

If the two objects are separated by a distance x_g on the ground, the corresponding echoes will be separated by a time difference Δt equal to:

$$\Delta t = \frac{2x_g \sin\theta}{c} \qquad \textbf{Equation 2.3 - 3}$$

The angle θ in Equation 2.3 - 3 is the local incidence angle. As the case of the slant range, the ground range resolution of the radar is given by

$$\tau = \frac{2x_g \sin\theta}{c} \implies x_g = \frac{c\tau}{2\sin\theta} \qquad \textbf{Equation 2.3 - 4}$$

From Equation 2.3 - 4 can be deduced that the local slopes in the image will affect the ground range resolution, since it is different for different incident angles. The effective pulse length can be described in terms of the system bandwidth B.

$$\tau = \frac{1}{B} \qquad \textbf{Equation 2.3 - 5}$$

Applying Equation 2.3 - 5into Equation 2.3 - 2, the slant range resolution can be rewritten as a function of the system bandwidth:

$$x_r = \frac{c}{2B} \qquad \textbf{Equation 2.3 - 6}$$

A pulse radar can determine the range by measuring the roundtrip time by transmitting a pulse signal. To enhance the signal to noise ratio, the energy in each pulse has to be increased. This can be done by increasing the transmitted peak power or by using a longer pulse, which results in a worse range resolution (see Equation 2.3 - 4). The solution to solve such restrictions is to use modulated pulses, which results in a wide bandwidth even when the pulse is very long. Chirp modulation is by far the most commonly used, which consists in vary the radar signal frequency linearly while the pulse is being transmitted.

Hitherto, it has been demonstrated that the cross-track resolution in the radar case is independent of the distance between the scene and the radar instrument and is a function of the system bandwidth.

Ap.4 Radar Equation

The SNR determines the quality of the radar imagery. The radar equation provides a relationship between the received power, the characteristics of the target and the characteristics of the radar.

The equivalent isotropic radiated power (EIRP) radiated by the transmitting antenna of the radar is:

$$P_{rad} = P_t G_t \qquad \textbf{Equation 2.4 - 1}$$

where $P_t$is the transmitted power and G_t the gain of the antenna. After traveling a distance R_1, the incident power density to the target is given by:

$$P_i = \frac{P_t G_t}{4\pi R_1^2}$$ **Equation 2.4 - 2**

The scattered power by the target is defined by the radar cross section σ of the target:

$$P_s = P_i \sigma$$ **Equation 2.4 - 3**

The scattered power density at the receiving antenna of the radar is defined as:

$$P_c = \frac{P_s}{4\pi R_2^2}$$ **Equation 2.4 - 4**

Finally, the received power depends on the *effective area* A of the receiver antenna:

$$P_{rec} = \frac{P_t G_t \sigma A}{(4\pi)^2 R_1^2 R_2^2}$$ **Equation 2.4 - 5**

In the case in which the transmitter and the receiver are at the same location, the term $R_1^2 R_2^2$ can be replaced by R^4.

In addition to the target echo, the received signal also contains noise. The components of the noise that are within the spectral bandwidth B of the sensor are passed through with the signal. The receiver electronics also generates noise that degrades the signal quality. Focusing on the effects of the thermal noise on the sensitivity of the system, the thermal noise power is given by:

$$P_N = kTB$$ **Equation 2.4 - 6**

where$k$ is Boltzmann's constant ($k = 1.6 \times 10^{-23}\, W/K/Hz$) and T is the total equivalent noise temperature in kelvin. The resulting SNR is:

$$SNR = \frac{P_r}{P_N}$$ **Equation 2.4 - 7**

Ap.5 Real Aperture Radar

The real aperture imaging radar uses an antenna that illuminates the surface to one side of the flight track. Such antenna illuminates a highly elongated elliptical shaped area on the surface, as shown in Figure 2 - 1. The angular beam width in the range plane for an antenna of width W is given by:

$$\theta_r \approx \frac{\lambda}{W}$$ **Equation 2.5 - 1**

And the resulting surface footprint is given by:

$$S \approx \frac{h\theta_r}{\cos^2\theta} = \frac{\lambda h}{W\cos^2\theta}$$ **Equation 2.5 - 2**

Where h is the sensor height above the surface and θ is the angle from the center of the illumination beam to the vertical (the look angle at the center of the swath).

The radar relies on the resolution of the antenna beam in the along-track direction for imaging. This means that such resolution is determined by the size of the antenna as well as the range to the scene. Assuming an antenna length of L, the antenna beam width in the along-track direction is

$$\theta_a \approx \frac{\lambda}{L}$$ **Equation 2.5 - 3**

At a distance R from the antenna, this means that the antenna beam width illuminates an area with the along-track dimension equal to

$$x_a \approx R\theta_a \approx \frac{\lambda R}{L} \approx \frac{\lambda h}{L\cos\theta}$$ **Equation 2.5 - 4**

In terms of the radar equation, the area responsible for reflecting the power back to the radar is given by the physical size of the antenna illumination in the along-track direction and the projection of the pulse on the ground in the cross-track direction. If the pulse has a length τ_p in time, and the signal is incident on the ground at an angle θ_i, the projected length of the pulse on the ground (ground range resolution) is

$$l_g = \frac{c\tau_p}{2\sin\theta_i}$$ **Equation 2.5 - 5**

The radar equation of a real aperture in terms of the physical antenna sizes can be written as

$$P_r = \frac{P_t W^2 L c\tau_p \sigma_0}{8\pi\lambda R^3 \sin\theta_i}$$ **Equation 2.5 - 6**

From Equation 2.5 - 6 can be seen that the received power increases as the square of the width of the antenna. However, increasing the antenna width also decreases the swath width. The received power increases linearly with an increase in the antenna length, which also improves the along-track resolution of the real aperture radar. For this reason, real aperture radars usually operate with antennas that are the longest that could be practically accommodated.

Ap.6 Synthetic Aperture Radar

"Synthetic aperture radar" is a coherent active microwave remote sensing technique that refers to a particular implementation of an imaging radar system that utilizes the movement of the radar platform and specialized signal processing to generate high-resolution images in both directions.

2.6.1 Ground-Based Synthetic Aperture Radar

Ground-based SAR (GBSAR) systems aim at obtaining 2D reflectivity images. The advantages of using a terrestrial platform are high stability, perfect knowledge of the sensor's track and no constraints of revisiting in time. The main drawback is related to its use on the earth surface, which limits the extension of the illuminated area and the maximum range distance that can be achieved (strong dependence with the geometry).

Frequency-modulated continuous wave (FM-CW) radars are commonly used in short-range applications [Skolnik, 90]. They offer some advantages such as the simpler hardware design, which implies lower costs, and the fact that the peak power of the signal is usually little greater than its average power.

Echoes received from the different positions are collected and coherently processed to retrieve reflectivity information of the scenario. In this chapter a theoretical description of the complete system is provided, from the transmitted signal generation to the focused image.

2.6.2 Range domain description

A Radar is an active system that radiates electromagnetic energy and detects the echoes returned from reflecting objects. When a target is illuminated by an electromagnetic wave, part of the energy is absorbed and the rest is scattered according to its geometrical and physical properties. As mentioned before, the transmitted signals are often modulated in order to enhance the spatial resolution of the system and the most commonly used is the chirp modulation. This modulation uses sinusoidal waveforms in which the frequency of the signal within the pulse is linearly changed as a function of the time. The resulting radar signal may be defined as

$$p(t) = \prod\left(\frac{t - T_p/2}{T_p}\right) e^{j\beta t + j\alpha t^2} \qquad \textbf{Equation 2.6 - 1}$$

where T_p is the chirp duration, α is the rate at which the angular frequency changes (chirp-rate) and the term β is the angular frequency carrier. The main advantage of this modulation is that high range resolution can be obtained without managing short-pulse high power peak signals, with relevant simplification of hardware devices [Skolnik, 90].

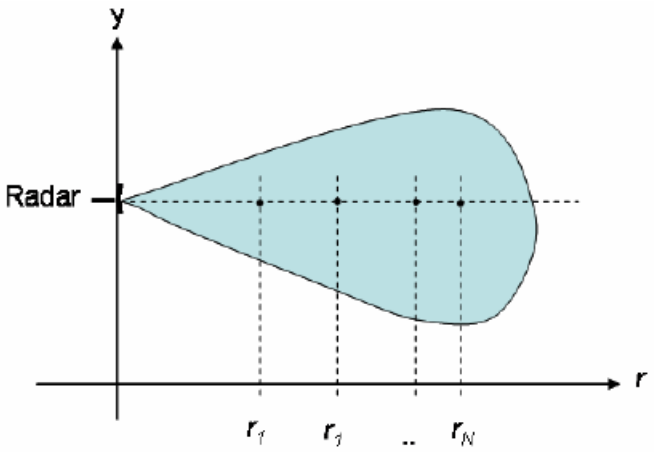

Figure 2 - 3 N point targets aligned along the *boreside* direction of the radar

Consider the two-dimensional scenario depicted in Figure 2 - 3, where N point targets are aligned along the range direction. The *radar cross section* (RCS) σ_n and the phase ϕ_n characterizes a generic point target n at a radial distance r_n, [Ishimaru, 78]. The complex reflectivity map function Γ of the scenario is

$$\Gamma(t) = \sum_{n=1}^{N} \sqrt{\sigma_n} e^{j\phi_n} \delta\left(t - \frac{2r_n}{c}\right) = \sum_{n=1}^{N} \sqrt{\sigma_n} e^{j\phi_n} \delta(t - t_n)$$

Equation 2.6 - 2

where the term t_n is the round-trip delay. When the signal illuminates the scene, the backscattered signal can be expressed as the convolution between Equation 2.6 - 1 and Equation 2.6 - 2 in the following way

$$\begin{aligned} s(t) &= \Gamma(t) * p(t) \\ &= \sum_{n=1}^{N} \sqrt{\sigma_n} e^{j\phi_n} \cdot p(t - t_n) \\ &= \sum_{n=1}^{N} \sqrt{\sigma_n} e^{j\phi_n} \prod \left(\frac{t - \left(T_p/2 + t_n\right)}{T_p} \right) e^{j\beta(t-t_n) + j\alpha(t-t_n)^2} \end{aligned}$$

Equation 2.6 - 3

$s(t)$ is the signal at the receiving antenna and is called *raw data* in signal processing. In Equation 2.6 - 3 the attenuation due to signal propagation is not taken into account for simplicity.

2.6.2.1 Matched filter vs deramping focusing

The matched filter is one of the most used techniques for range-domain focusing purposes and is the optimal solution to maximize the SNR in presence of additive stochastic noise [Curlander, 91]. This technique convolves the backscattered signal with the conjugated time-reversed version of the transmitted signal to detect the common elements between both.

$$s_M(t) = s(t) * p^*(-t) = \sum_{n=1}^{N} \sqrt{\sigma_n} e^{j\phi_n} h(t - t_n)$$

Equation 2.6 - 4

Where $h(t)$ is the *point spread function (psf)*. The psf describes the response of the range imaging system and is defined as

$$h(t) = \mathcal{F}^{-1}[|P(w)|^2]$$

Equation 2.6 - 5

where $P(w)$is the Fourier transform of the transmitted signal. The function $h(t)$ is mainly related to the bandwidth of the transmitted signal and therefore, according to Equation 2.3 - 6, is related to the range resolution and the capability to resolve targets in the range dimension. Most of the pulsed SAR sensors use the matched filter to perform the range-processing of the raw data.

An alternative technique, which is used in the UPC SAR system, is the deramping technique [Soumek, 99]. From a mathematical point of view, it consists in multiplying the conjugated received signal by the phase term of the chirp in Equation 2.6 - 1, yielding

$$s_c(t) = s^*(t) e^{j\beta t + j\alpha t^2}$$
$$= \sum_{n=1}^{N} \sqrt{\sigma_n} e^{j\phi_n} \prod\left(\frac{t - (T_p/2 + t_n)}{T_p}\right) e^{j(\beta t_n - \alpha t_n^2)} e^{j\alpha t_n t}$$

Equation 2.6 - 6

The sinusoid $e^{j\alpha t_n t}$ gives the information of the target's position. The carrier β and the chirp-rate α introduce an absolute phase offset related with the round-trip delay. Denoting F as the Fourier transform, the range-compressed response from the illuminated scene may be obtained by transforming Equation 2.6 - 6 as follows

$$S_c(w) = F[s_c(t)] =$$
$$\sum_{n=1}^{N} \sqrt{\sigma_n} e^{j\phi_n} e^{j(\beta t_n + \alpha t_n^2 - w t_n)} H\left(w - \frac{4\alpha r_n}{c}\right) = \sum_{n=1}^{N} S_{cn}(w)$$

Equation 2.6 - 7

Where $H(w)$ is the deramped *psf* equal to

$$H(w) = F\left[\prod\left(\frac{t - (T_p/2)}{T_p}\right)\right] = T_p sinc(wT_p)$$

Equation 2.6 - 8

The deramping and the matched filter technique have approximately the same properties in resolving targets in the range domain. Nonetheless, despite the amplitude term given by the two techniques is almost equivalent, the absolute phase significantly changes. While in the matched filter $h(t)$ is modulated by $e^{j\phi_n}$, the deramping process introduces additional phase terms related to the target's range location.

2.6.2.2 Saw-tooth cosine chirp in continuous wave (CW) radar

The GBSAR sensor developed by the Remote Sensing Lab at UPC consists of a FM-CW radar. The system generates a cosine-chirp signal and the deramping process is done at hardware level by beating the received signal with the transmitted one. According to radar technology [Skolnik, 90], a high SNR can be obtained by repeating continuously the signal modulation and by successively time-averaging the collected echoes.

In this section, the spectral features of the deramped signal will be analyzed when a real chirp is transmitted. For the sake of simplicity, only one modulation is considered. The cosine-chirp transmitted signal can be expressed as

$$p(t) = Re\{a(t)e^{j\beta t + j\alpha t^2}\} = a(t)\cos(\beta t + \alpha t^2) \qquad \textbf{Equation 2.6 - 9}$$

The backscattered signal by the nth target is

$$s(t) = \left[\sqrt{\sigma_n}e^{j\phi_n}a(t-t_n)\cos(\beta(t-t_n) + \alpha(t-t_n)^2)\right] \qquad \textbf{Equation 2.6 - 10}$$

As mentioned before, the deramping process implemented at hardware level multiplies the received signal (Equation 2.6 - 10) with the transmitted one (Equation 2.6 - 9).

$$s_c(t) = s(t)\cdot p(t)$$

$$= \left[\sqrt{\sigma_n}e^{j\phi_n}a(t-t_n)\cos(\beta(t-t_n) + \alpha(t-t_n)^2)\cos(\beta t + \alpha t^2)\right] \qquad \textbf{Equation 2.6 - 11}$$

By applying the Euler's formula $\cos(a)\cos(b) = \frac{1}{2}(\cos(a+b) + \cos(a-b))$, the deramped signal in the time domain $s_c(t)$ can be discomposed in two terms

$$s_c(t) = \frac{1}{2}\sqrt{\sigma_n}e^{j\phi_n}a(t-t_n)\cdot$$

$$[\cos(2\beta t - \alpha t t_n + \alpha t^2 - \beta t_n + \alpha {t_n}^2) + \cos(-\alpha t t_n - \beta t_n + \alpha {t_n}^2)] \qquad \textbf{Equation 2.6 - 12}$$

After lowpass filtering the deramped signal $s_c(t)$, the baseband received signal is obtained

$$s_c(t) = \frac{1}{2}\sqrt{\sigma_n}e^{j\phi_n}a(t-t_n)[\cos(-\alpha t t_n - \beta t_n + \alpha {t_n}^2)] \qquad \textbf{Equation 2.6 - 13}$$

The range Fourier transform is given by

$$S_c(\omega,u)=\int_{-\infty}^{\infty}s_c(t)\,e^{-j\omega t}dt$$

$$=\frac{1}{4}\sqrt{\sigma_n}e^{j\phi_n}e^{-j\beta t_n}e^{j\alpha {t_n}^2}\int_{-\infty}^{\infty}a(t-t_n)\,e^{-j\alpha t t_n}e^{-j\omega t}dt$$

$$=\frac{1}{4}\sqrt{\sigma_n}e^{j\phi_n}e^{-j\beta t_n}e^{j\alpha {t_n}^2}e^{-j\omega t_n}A(\omega+\alpha t_n)$$

Equation 2.6 - 14

where $A(\omega)=\mathcal{F}\big(a(t)\big)$.

2.6.2.3 Residual video phase (RVP) error estimation

The use of the deramping process generates several phase terms that depend on the target's range distance. From Equation 2.6 - 7, the range contribution of the range-compressed signal $S_c(w)$ from the *n*th target is

$$\angle S_{cn}(w)=\phi_n+\beta t_n+\alpha {t_n}^2-\omega t_n+\angle H(\omega-2\alpha t_n)$$ **Equation 2.6 - 15**

The term ϕ_n is related to the target's backscattering properties and the term $+\angle H(\omega-2\alpha t_n)$ is determined by the characteristics of the system. The *Residual Video Phase (RVP)* error, which is an undesired term, is represented by $\alpha {t_n}^2$. The RVP and the term βt_n must be removed because have undesired effects on the SAR imaging due to its variations with the round-trip time delay. The general relation between the angular frequency ω and the range r is given by

$$\omega=\alpha t=\frac{4\alpha r}{c}$$ **Equation 2.6 - 16**

If a continuous sampling of $s_c(t)$ is done, it would be possible to estimate the frequency ω_n corresponding to the exact position of the target r_n and fulfilling the condition

$$\omega_n t_n=2\alpha t_n^2$$ **Equation 2.6 - 17**

The absolute phase of *psf* describing the location of the target simplifies to

$$\angle S_{cn}(w)=\phi_n+\beta t_n-\alpha {t_n}^2$$ **Equation 2.6 - 18**

And the compensation of the term $-\alpha {t_n}^2$ would be trivial. Considering a sampled version of $s_c(t)$, the absolute phase description in the discrete domain must be reformulated and Equation 2.6 - 18 becomes

$$\angle S_{cn}(k_{MAX}\Delta w) = \phi_n + \beta t_n - \alpha {t_n}^2 - k_{MAX}\Delta w t_n + \angle H[k_{MAX}\Delta w - 2\alpha t_n] \quad \textbf{Equation 2.6 - 19}$$

where Δw is the angular frequency increment and k_{MAX} represents the index of the closest sample to the real position of the target in the range-compressed profile. The last term in Equation 2.6 - 19 can be neglected simplifying the expression to

$$\angle S_{cn}(k_{MAX}\Delta w) = \phi_n + \beta t_n - \alpha {t_n}^2 + \Delta Q \quad \textbf{Equation 2.6 - 20}$$

Where ΔQ is the quantization error given by

$$\Delta Q = 2\alpha {t_n}^2 - k_{MAX}\Delta w t_n \quad \textbf{Equation 2.6 - 21}$$

It is convenient to express ΔQ as a function of the system parameters to analyze the effects of the time-sampling step on the *RVP* error compensation. With this objective, some comments about the time-sampling of $s_c(t)$ can be done. Being the position of a target associated to an angular frequency component (Equation 2.6 - 16), the radar maximum range is limited by the maximum alias-free sampled frequency ω_{rmax}. If the GBSAR system acquires N number of time-samples during the chirp time-length T_p, the time sample step Δt results

$$\Delta t = \frac{T_p}{N-1} = \frac{T_p}{N} \text{ for } N \gg 1 \quad \textbf{Equation 2.6 - 22}$$

The corresponding sampling angular frequency w_s and the maximum ω_{rmax} are

$$w_s = \frac{2\pi}{\Delta t} \backsimeq \frac{2\pi T_p}{N} \quad \textbf{Equation 2.6 - 23}$$

$$\omega_{rmax} = \frac{w_s}{2} = \frac{\pi T_p}{N-1} \backsimeq \frac{\pi T_p}{N} \Longrightarrow r_{max} = \frac{c\omega_{rmax}}{4\alpha} \backsimeq \frac{c\pi T_p}{4\alpha N} \quad \textbf{Equation 2.6 - 24}$$

The frequency separation Δw between successive elements of $S_c(\omega)$ is related to the observation period of the signal T_p in the time domain and results

$$\Delta w = \frac{\omega_{rmax}}{N/2} = \frac{w_s/2}{N/2} \backsimeq \frac{2\pi}{T_p} \quad \textbf{Equation 2.6 - 25}$$

The range resolution is the given by

$$\Delta r = \frac{\Delta w c}{4\alpha} = \frac{c\pi}{2\alpha T_p} \quad \textbf{Equation 2.6 - 26}$$

Which corresponds to the general expression given in Equation 2.6 - 1. Defining the mth non-null samples of $s_{cn}(t)$

$$s_{cn}[m] = \sqrt{\sigma_n} e^{j\phi_n} e^{j\beta t_n - \alpha t_n^2 + j2\alpha t_n m\Delta t} m = 1,2,\dots,N \quad \textbf{Equation 2.6 - 27}$$

The kth element of $S_c(\omega)$ is given by the *Fast Fourier Transform* (FFT) of Equation 2.6 - 27 and is equal to

$$s_{cn}[k] = \sum_{m=0}^{N-1} s_{cn}[m] e^{-j\frac{2\pi}{N}km} = \sqrt{\sigma_n} e^{j\phi_n} e^{j\beta t_n - \alpha t_n^2} \sum_{m=0}^{\boldsymbol{N-1}} e^{j\frac{2m}{N}(\alpha t_n T_p - \pi k)} \quad \textbf{Equation 2.6 - 28}$$

The index k_{MAX} identifying the position of the nth target corresponds to the value of k maximizing the sum in Equation 2.6 - 28 and minimizing the quantity $\alpha t_n T_p - \pi k$. It follows that the quantization error ΔQ introduced by the *RVP* is related to this difference and becomes null only in the case that the frequency $2\alpha t_n$ is sampled exactly. Since target's position is unknown, this condition cannot be guaranteed for any index k. This way, the smaller the term Δw, the smaller the quantization error. Theoretically, this can be achieved via hardware by extending the chirp time duration, but an easier solution is to interpolate the compressed signal before the compensation of the *RVP* error. The interpolation technique usually used is the so called *zero-padding*.

In order to quantify the improvement in the reconstruction of the absolute phase, a term describing the interpolation step must be introduced in the formulation. Denoting with f_z the zero-padding factor, Equation 2.6 - 33 may be modified as follows

$$s_{cn}[k] = \sqrt{\sigma_n} e^{j\phi_n} e^{j\beta t_n - \alpha t_n^2} \sum_{m=0}^{\boldsymbol{N-1}} e^{j\frac{2m}{f_z N}(\alpha t_n f_z T_p - \pi k)} \quad \textbf{Equation 2.6 - 29}$$

The analytical solution of Equation 2.6 - 29 [Proakis, 98] leads to rewrite Equation 2.6 - 20 as

$$\angle S_{cn}(k) = \phi_n + \beta t_n - \alpha {t_n}^2 + \frac{N-1}{f_z N}\left(\alpha t_n f_z T_p - \pi k\right) \text{ for } k = 1,2,\dots,Nf_z \quad \textbf{Equation 2.6 - 30}$$

and the index identifying the range position of the target is then given by

$$k_{MAX} = round\left(\frac{\alpha t_n f_z T_p}{\pi}\right) \quad \textbf{Equation 2.6 - 31}$$

Theoretically, the higher the interpolation factor, the lower the value of ΔQ. In short-range systems like the UPC GBSAR it has been observed that, for values of $f_z \geq 16$, negligible improvements are achieved. The Range Cell Migration (RCM) effect, that produces a displacement in the range position as the radar moves linearly in the platform and will be described in the cross-range domain description, can also be negligible with a $f_z \geq 16$. Accordingly, it is meaningful to define a correction function $F[k]$ equal to

$$F[k] = e^{j\alpha\left(\frac{\Delta w k}{2\alpha}\right)^2} \text{ for } k = 1,2,\dots,Nf_z \quad \textbf{Equation 2.6 - 32}$$

and the interpolated compressed signal compensated for the RVP error $S_c^{RVP}[k]$ is finally obtained as

$$S_c^{RVP}[k] = S_c[k]F[k]$$

Since RVP error is related just to the deramping process, the same $F[k]$ is used for the whole synthetic aperture.

2.6.3 Cross-range domain description

In SAR data, the so called *range* dimension is related to the propagation time of the echoed signals. As these signals propagate at the speed of light such dimension is usually referred as *fast-time* domain. Otherwise, the azimuth or *cross-range* dimension is related to the speed of the platform in which the radar system is boarded and it is usually referred as *slow-time* domain. As mentioned before in this chapter, the term synthetic aperture is derived from the acquisition procedure, based on the movement along a linear trajectory of the radar system. With synthetic aperture radar an imaginary aperture much longer than the physical dimensions of the receiving and transmitting antennas is synthetized. The collection of echoes in the cross-range domain provides the necessary information to retrieve bidimensional complex images of the illuminated scene.

2.6.3.1 Cross-range domain: classical formulation

Consider the geometry shown in Figure 2 -4.

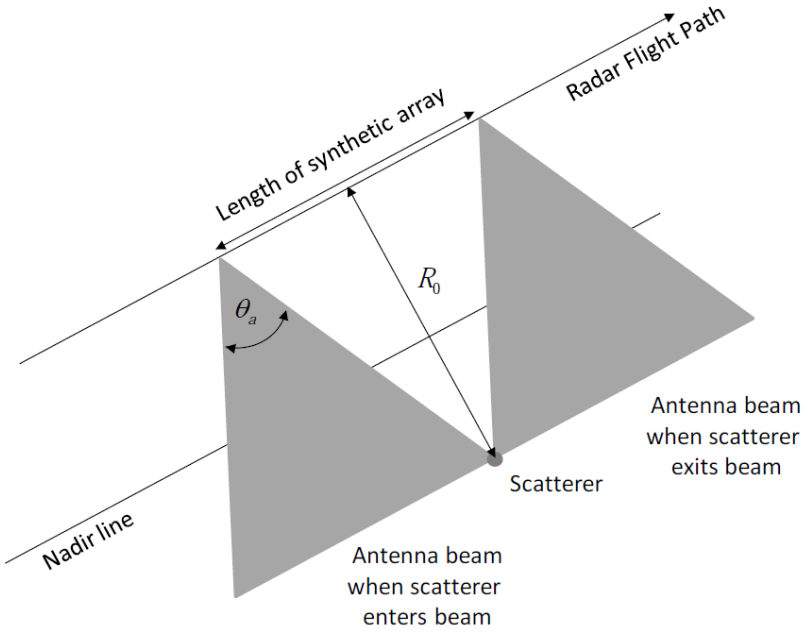

Figure 2 -4 The synthetic aperture radar operation

As the radar moves along the flight path, the distance between the radar and the scatterer changes. The phase of the radar signal is given by $-4\pi R(s)/\lambda$. Because of the changing distance between the radar and the scatterer, the phase of the signal after range compression will be different for every position of the radar. This changing distance can be written as

$$R(t) = \sqrt{R_0^2 + v^2 t^2}$$ **Equation 2.6 - 33**

where$R_0$is the range at closest approach to the scatterer, v is the velocity of the radar platform and t is the time along the flight path (so called slow time) with zero time at the time of closest approach. Using the approximation $vt << R_0$, the range as a function of the slow time can be written as

$$R(t) \approx R_0 + \frac{v^2}{2R_0} t^2$$ **Equation 2.6 - 34**

The quadratic term in Equation 2.6 - 34 introduces the so-called *range cell migration* (RCM) effect and describes the geometric locus of points that the signal energy from a punctual scatterer follows the two-dimensional SAR data. This effect is related to the changing range delay to the target as it passes through the antenna beam and may introduce shifts of several range bins. In the classical SAR formulation, the RCM is the same for targets characterized by the same zero-Doppler, and increases with R_0. The phase of the backscattered signal after range compression is

$$\emptyset(t) = -\frac{4\pi R(t)}{\lambda} \approx -\frac{4\pi R_0}{\lambda} - \frac{2\pi v^2}{R_0 \lambda} t^2$$ **Equation 2.6 - 35**

The instantaneous frequency of this signal is

$$f(t) = \frac{1}{2\pi} \frac{\partial \phi(t)}{\partial t} = -\frac{2v^2}{R_0 \lambda} t$$ **Equation 2.6 - 36**

This is the expression of a linear frequency chirp. To find the bandwidth of this signal, the time that the scatterer is within the antenna beam is used to find the maximum “integration time”. For an antenna with a physical length L, the half-power horizontal beam width is $\theta_a = \lambda / L$, so that the scatterer at the range of closest approach R_0 is illuminated for a time

$$t_{tot} = \frac{\lambda R_0}{Lv}$$ **Equation 2.6 - 37**

Half of this time occurs when the radar is approaching the range of closest approach and half of it occurs when travelling away from such range. Therefore, the Doppler bandwidth of the SAR signal in Equation 2.6 - 36 is

$$B_D = \frac{2v}{L}$$ **Equation 2.6 - 38**

It can be noticed that B_D does not depend on target’s zero-Doppler position R_0 but only on two physical parameters of the system: the platform’s speed v and the physical dimension of the antenna L. If this signal is filtered with a matched filter, the resulting signal will have a

width in time of $1/B_D$. The resolution of the synthetic aperture technique in the cross-range dimension can be directly obtained from the azimuth bandwidth as

$$\Delta_a = \frac{v}{B_D} = \frac{L}{2} \qquad \textbf{Equation 2.6 - 39}$$

The Equation 2.6 - 39 represents the most important achievement of radar imaging provided by the synthetic aperture technique. This result shows that the azimuth resolution for synthetic aperture radar is equal to half the size of the physical antenna and is independent of the distance between the sensor and the target. It also demonstrates that a smaller antenna gives better resolution. This is because the smaller the physical antenna is, the larger its footprint. This allows a longer observation time for each point on the surface (i.e., a longer array can be synthesized). This longer synthetic array allows a larger Doppler bandwidth and, hence, a finer surface resolution. Similarly, if the range between the sensor and the surface increases, the physical footprint increases, leading to a longer observation time and larger Doppler bandwidth, which counterbalances the increase in the range. The independence between the azimuth bandwidth Δ_a and the distance between the sensor and the target is exploited by the main cross-range focusing algorithms: the range-Doppler, the wavenumber or $\omega - k$ and the Chirp-scaling algorithms.

Among the processing techniques mentioned before, none of them are suitable for cross-range focusing the UPC sensor. The classical range-Doppler and chirp-scaling/extended chirp-scaling algorithms do not represent an optimal solution when wide-beam antennas are employed and, consequently, high squinted observations are gathered. Regarding $\omega - k$, it is unsuitable to focus UPC sensor's raw data. The presence of the term $\alpha t_n t$ described in Equation 2.6 - 6, which represents the kernel of range focusing process, makes the base-band hypotheses of range-compressed raw data fail.

The Back-Projection (BP) is a general cross-range focusing algorithm that has no specific assumption about raw data spectral properties [Soumek, 99]. With this method the exact inversion of linear-aperture SAR problem under any observation geometry can be done, either if it is very large(high-resolution SAR) or very short (terrestrial SAR sensor) [Prats, 05]. Essentially it constitutes a generalization of classical beam-forming: for each image pixel the expected signal is used as a reference kernel in a correlation processing. The equivalent pulse echo is interpolated at time-delay corresponding to the range between the pixel and each position of the antenna and back-projected to the position in the image grid. The pixel-by-pixel sum of the interpolated values directly provides the final focused image. The two main drawbacks of the BP technique are the poor computational efficiency and the high interpolation rate of the range-compressed raw data needed for an accurate retrieval of the scenario reflectivity map. But if the BP is usually discarded for airbone and satellite acquisitions processing, it turns out to be suitable for the UPC sensor's raw data. Moreover, it takes advantage of the high interpolation factor required to remove the RVP error discussed in section2.6.2.3. It also benefits of the small scenario and the fixed observation geometry to reduce the computational time.

2.6.3.2 The Back-Projection Focusing Algorithm

Let $P_T(x_T, y_T, z_T)$ define the position of a generic target T in the system reference sketched in Figure 2 -4 and R_0 is the zero-doppler distance. According to Equation 2.6 - 2 and Equation 2.6 - 7, the RVP compensated backscattered signal from T when the sensor is located at $P_s(0, u, 0)$ can be expressed as

$$S_c^{RVP}(\omega, u) = \psi(R_0, y_T) e^{j\frac{2\beta}{c}\sqrt{R_0^2+(y_T-u)^2}} H\left(\omega - \frac{4\alpha}{c}\sqrt{R_0^2 + (y_T - u)^2}\right) \quad \textbf{Equation 2.6 - 40}$$

where $\sqrt{\sigma_n e^{j\emptyset_n}}$ has been here substituted by the complex reflectivity function $\psi(R_0, y_T)$, defined for any point within the swath. Denoting with L the length of the synthetic aperture and R_{ref} the reference distance chosen to carry out the in-phase sum of backscattered echoes, an estimation of $\psi(r_T, y_T)$ may be obtained as

$$\hat{\psi}(R_0, y_T) e^{j\frac{4\pi}{\lambda}R_{ref}} = \int_{-L/2}^{L/2} S_c^{RVP}\left(\omega - \frac{4\alpha}{c}\sqrt{R_0^2 + (y_T - u)^2}, u\right) \zeta(u, R_0, y_T) du \quad \textbf{Equation 2.6 - 41}$$

where

$$\zeta(u, R_0, y_T) = Ae^{-j[sign(\alpha)]\frac{2\beta}{c}\left(\sqrt{R_0^2+(y_T-u)^2} - R_{ref}(R_0, y_T)\right)} \quad \textbf{Equation 2.6 - 42}$$

is usually referred as *back-projection* kernel. The function $sign(\alpha)$ must be introduced to make the phase of the compensation kernel consistent with the sign of the *chirp-rate*. In classical formulation, R_{ref} corresponds to the zero-Doppler distance R_0 [Soumeck, 99].

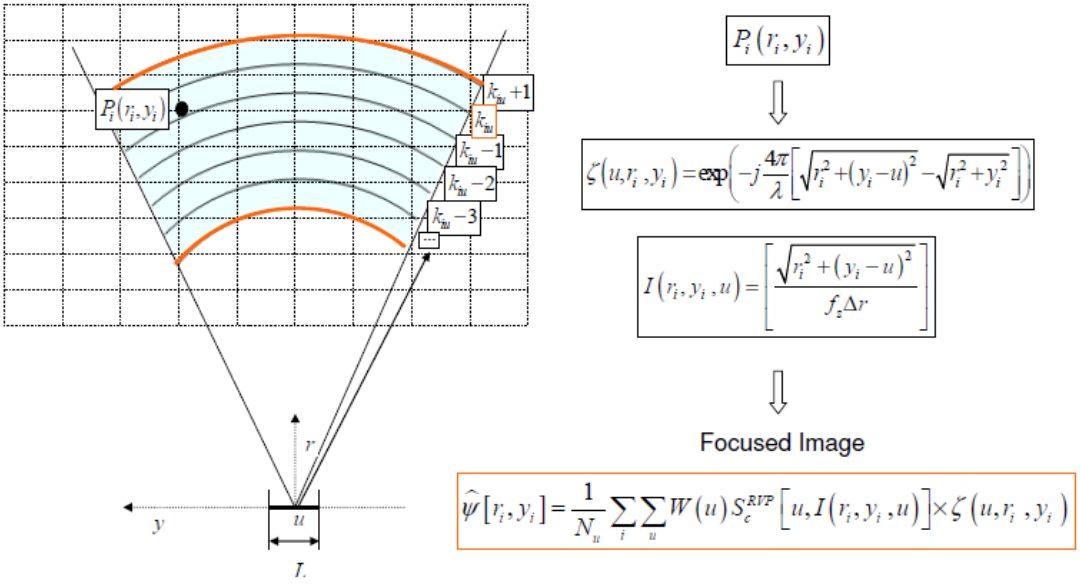

Figure 2 - 5 Graphical description of back-projection focusing algorithm

The complex reflectivity image is finally obtained by defining a grid $\hat{\psi}(R_0, y_T)$ in the (R_0, y) 2D domain and solving the integral Equation 2.6 - 41 at each point of the grid. As the range sampling does not follow targets' range migration, the range-compressed data is usually interpolated to obtain a precise computation of Equation 2.6 - 41. Concerning the case of the UPC system, the interpolation step is carried out for the removal of the RVP error. Then the signal S_c^{RVP} in Equation 2.6 - 40 can be directly projected onto the image grid.

It is worth noting that no limitation has been introduced in the (r_T, y_T) domain. The reason lies in the physical meaning of the back-projection process, which spreads out the interpolated range-compressed radar echo like a fan each time centered on the proper antenna phase center and sums them coherently. Accordingly, the integral in Equation 2.6 - 41 can be evaluated for an arbitrary image position or size and at any resolution scale. This fact makes it possible to handle any aperture geometry, either very large (high-resolution SAR) or very short (terrestrial SAR sensor).

Analyzing the computational cost of the BP, if N positions of the aperture are to be examined for each of the NxN pixels of the final image, this number is proportional to N^3. The computational cost can be reduced to $N^2 logN$ by multi-stages algorithms operating in the time-domain [Yegulalp, 99], which basically exploit the fundamental redundancy between nearby aperture positions for high-frequency reflectivity components in the along-track direction. The rationale fast back-projection (FBP) approaches is still dividing the full-aperture into sub-apertures to be processed in parallel and achieve an efficiency of $N^2\sqrt{N}$ [Urlander, 03].

Despite these improvements, the BP technique still remains unattractive for wide-area processing and it is just employed to obtain reference images for the assessment of faster focusing methods. On the contrary, BP constitutes the optimum solution for GBSAR acquisitions. BP is able to handle the spatial variance of the pixels' spectral properties and besides the computation time becomes more than tolerable due to the small scene that the terrestrial platform can illuminate. Besides, this computational time can be reduced when a high number of data sets acquired with a fixed geometry are to be processed. In fact, cross-range samples are taken at the same positions along the linear unit during the repeated scanning processes. Then, two look-up tables can be created: $[I]$, which contains the position of the useful information in each line of the interpolated range-compressed 2D raw data, and $[\zeta]$, that provides the value of the kernel compensating for each variation of the target-to-sensor time-delay. Figure 2 - 5 explains how the two matrices are created. Up to this point, Equation 2.6 - 41 can be rewritten for the discrete domain as

$$\hat{\psi}[R_0, y_i] = \frac{1}{N_u} \sum_u W(u) S_c^{RVP}[u, I(R_0, y_i, u)] \times \zeta\,(u, R_0, y_i) \qquad \textbf{Equation 2.6 - 43}$$

Where the index i identifies the image pixel, u the position of the sensor along the aperture and $W(u)$ accounts for the filtering window employed for the cross-range side-lobe suppression. A description of different filtering windows that may be employed to reduce side-lobes generated by the BP can be found in [Levanon, 04].

2.6.3.3 Cross-range sampling condition

According to the SAR classical formulation [Soumek, 99], the maximum cross range bandwidth Ω_T characterizing a target in the case of isotropic Tx/Rx antennas and an infinite synthetic aperture L is given by

$$\Omega_T = -2k\sin\theta_T\left(\frac{L}{2}\right), 2k\sin\theta_T\left(\frac{L}{2}\right)\Big|_{L\to\infty} = [-2k, 2k] \qquad \textbf{Equation 2.6 - 44}$$

For an alias-free cross-range imaging over the whole 2D radar plane, the Nyquist's criterion states that

$$2k_{MAX} \le \frac{2\pi}{\Delta u} \Longrightarrow \Delta u \le \frac{\pi}{2k} = \frac{\lambda}{4} \qquad \textbf{Equation 2.6 - 45}$$

where Δu is the cross-range maximum sampling step. Nonetheless, the Nyquist's condition turns out to be too restrictive for real acquisitions where antennas with limited cross-range beam are employed. As a first approximation, the maximum cross-range sampling step that can be accepted is given by

$$\Delta u \le \frac{\pi}{2k\sin\theta_{MAX}} \cong \frac{\pi}{k\Delta\Omega_0} \qquad \textbf{Equation 2.6 - 46}$$

Equation 2.6 - 46 has been directly derived from Equation 2.6 - 45 for the *stripmap* acquisition mode. In the case of squinted observation, i.e. when antennas' cross-range direction is not orthogonal to sensor's trajectory but tilted of an angle θ_c, Equation 2.6 - 46 is substituted by a more general expression [Soumek, 99] equal to

$$\Delta u \le \frac{\pi}{k\sin\theta_{MAX} - k\sin\theta_{MIN}} = \frac{\pi}{k\sin(\Delta\Omega_0/2 + \theta_c) - k\sin(\Delta\Omega_0/2 - \theta_c)} \qquad \textbf{Equation 2.6 - 47}$$

In the case of GBSAR systems, the short synthetic aperture prevents from employing so narrow beam antennas for gathering useful observations. Accordingly, wider cross-range illumination cones are usually preferred. In this case, Equation 2.6 - 46 is still valid but θ_{MAX} becomes now the maximum angular position where a target can be clearly detected by the Tx/Rx antennas. The reason is again related to the short dimension of the synthetic aperture. For satellite or air-borne platforms, only the samples obtained when the target passes through the nominal beam width (-3dB) are characterized by a useful S/N ratio, while the rest of contributions are too noisy and do not significantly contribute to the focusing process. Contrarily, the short range distance of targets illuminated by GBSAR sensors and the time-average operation performed by the FM-CW radar technology guarantee a high S/N ratio even for angular sectors wider than $\Delta\Omega_0$. It follows that imposing the condition $\theta_{MAX} > \Delta\Omega_0/2$ represents the only way to retrieve alias-free information concerning the scene that the sensor is observing efficiently, which turns out to be wider than the area within the -3dB antenna beam.

2.6.3.4 Foreshortening, layover and shadowing effect in GBSAR images

The radar system measures distances in the slant range direction so that all the ground features are sorted as a function of their distance to the sensor. This leads to some typical slant range distortion phenomena that affect SAR imaging independently of the type of platform employed for the measurement.

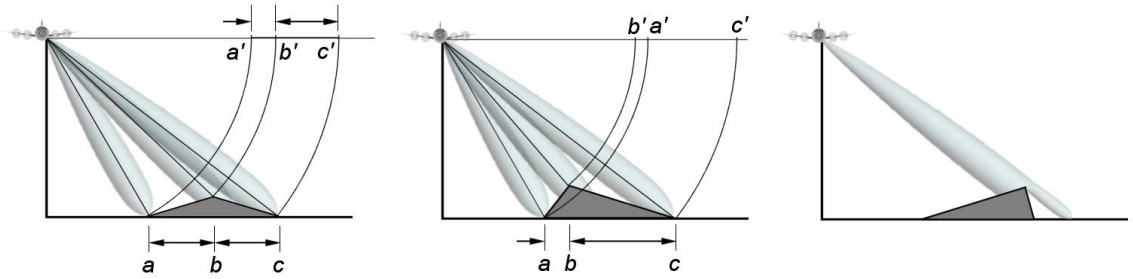

Figure 2 - 6 Distortion effects of foreshortening (left), layover (center), and shadowing (right) phenomena in SAR imaging process

Foreshortening occurs when the radar beam reaches the base of a tall feature tilted towards the radar (e.g. a mountain) before it reaches the top. Because the radar measures distance in slant-range, the slope (from point a to point b in Figure 2 - 6 left) will appear compressed and the length of the slope will be represented incorrectly (a' to b' in Figure 2 - 6 left) at the image plane. When the radar beam reaches the top of a tall feature (b in Figure 2 - 6 center) before it reaches the base (a), the effect called *layover* occurs. The returned signal from the top of the feature will be received before the signal from the bottom. As a result, the top of the feature is displaced towards the radar from its true position on the ground, and “lays over” the base of the feature (b' to a' in Figure 2 - 6 center). Finally, terrain slopes with an inclination lower than the incident angle are not illuminated as can be seen in Figure 2 - 6 right. As they appear as noisy dark areas in the focused SAR image, this effect is called *shadowing*.

In general, terrestrial sensors work with incident angles much higher than satellite and air-borne platforms, so foreshortening and shadowing are likely to affect the GBSAR acquisitions significantly. Since the observation geometry of GBSAR sensors strictly depends on its specific location with respect to the area of interest, its deployment must be chosen cautiously in order to optimize quality of monitoring conditions.

Oscillation of an Scatterer and its Influence in the Focused Image

3.1 Introduction to oscillation of an scatterer

The observation time of an acquisition in a SAR system is an important parameter that will determine the quality of the focused image. Some effects have been studied in this context such as the ground clutter introduced by the scintillation of the vegetation during a SAR measurement. The scintillation effect will be analyzed in detail in the next chapter.

In this chapter, the effect of the oscillation of a target in the range direction, which implies a variation of the distance from the sensor to the object, and its impact in the focused image will be studied. For this purpose, some simulations have been performed to corroborate the effects observed in the measurements. Measurements with the X band UPC SAR sensor and the W band UPC SAR sensor have been performed.

3.2 X Band GBSAR simulations and measurements

3.3.1 Effects of the oscillation of an object in the image

An oscillating object present in the radar field of view during a SAR acquisition has an impact in the final focused image. To evaluate, as a first approximation, the effects in the image of the oscillation of an object measured by the SAR system, a simulator has been developed. The simulator reproduces an equivalent of a real raw data matrix and applies the BP algorithm to obtain the focused image. Figure 3 - 1 shows a static target at a distance of 350 m in the range direction. To evaluate the oscillation of such target in Figure 3 - 1, a displacement in its position is applied; concretely a cosine function in the range direction. Two different oscillation periods of the cosine function and two different amplitudes will be evaluated. First, a cosine of 2.1 period oscillation during the interval of measurement with an amplitude of 15 mm and 30 mm will be evaluated and second a cosine ten times faster with an amplitude of 15 mm and 30 mm. The parameters considered for the simulations are a central frequency of 9.65 GHz, a bandwidth of 100 MHz, a *pulse repetition frequency* (PRF) of 20 KHz and a chirp-rate of $100\ MHz/100\ \mu s$.

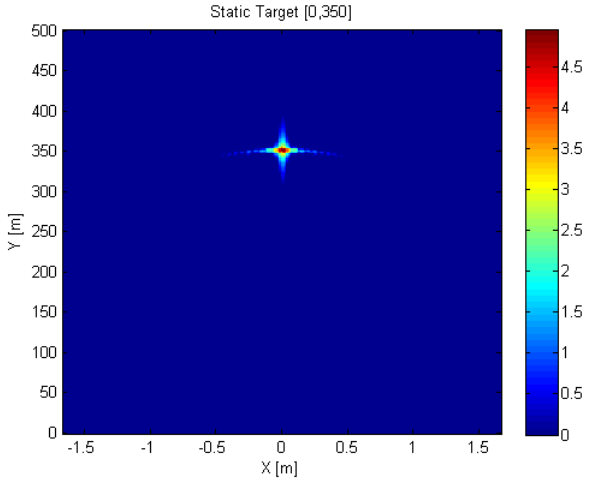

Figure 3 - 1 Simulated target at position [0,350]

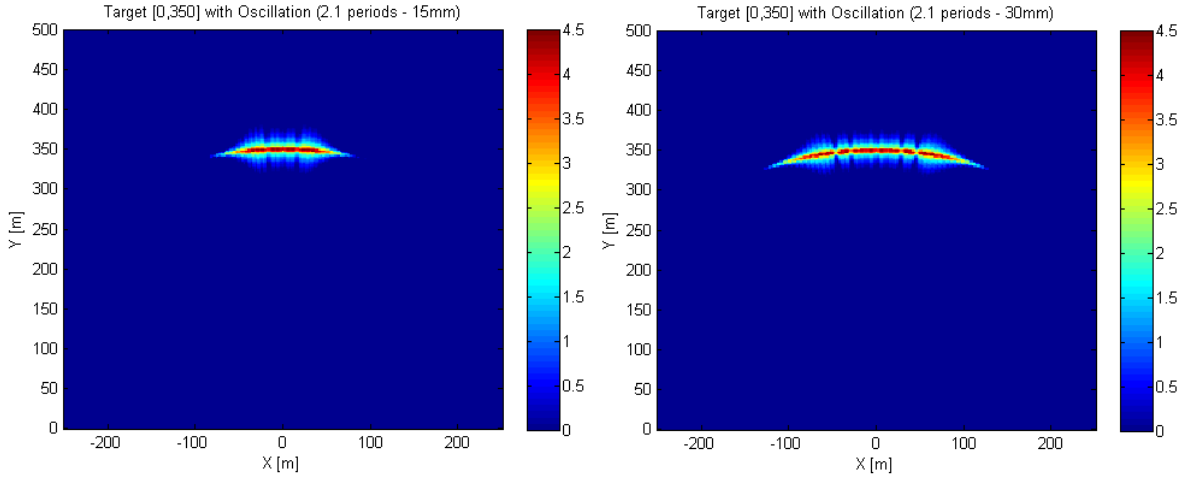

Figure 3 - 2 Left: 2.1 periods oscillation, 15 mm amplitude. Right: 2.1 periods oscillation, 30 mm amplitude

In Figure 3 - 2 an important spreading of the pixel of the target at the same radial range is observed. As the amplitude of the oscillation increases, the spreading is more accentuated.

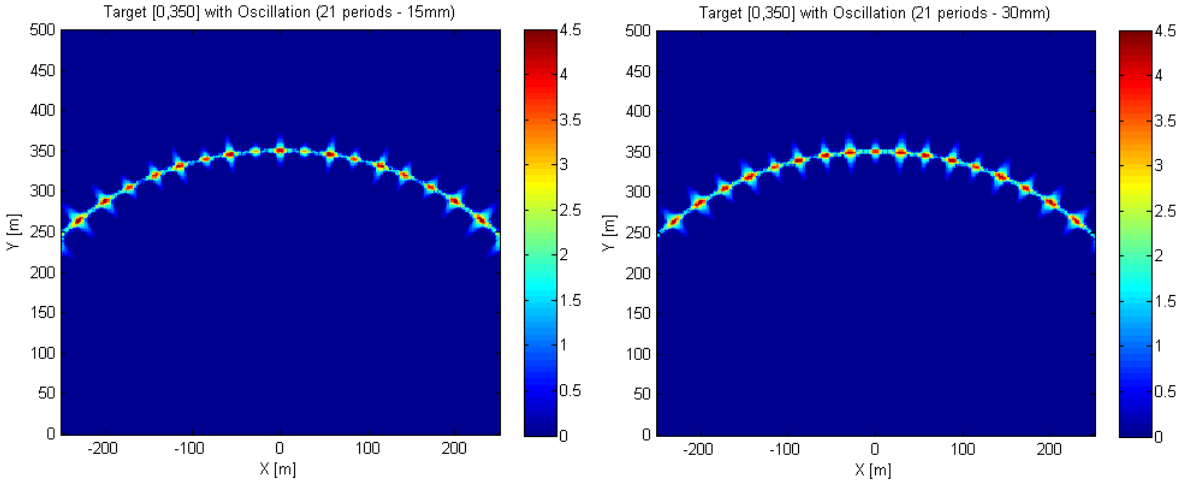

Figure 3 - 3 Left: 21 periods oscillation, 15mm amplitude. Right: 21 period oscillation, 30mm amplitude

In Figure 3 - 3 a new phenomenon with respect to Figure 3 - 2 is observed. As the oscillation period of the object is too fast, the received signal is subsampled and different replicas of the main target appear. Besides, as the amplitude of the oscillation increases the replicas are more accentuated. In both cases, the real position of the target is masked by the spreading in Figure 3 - 2 and the replicas in Figure 3 - 3.

To evaluate the phenomenon observed in the simulations, a measurement with the stop and go technique has been realized from the roof of the UPC to the Collserola range, in the outskirts of Barcelona (Figure 3 - 4). During the measurement of Figure 3 - 5, a crane with high reflectivity was located at approximately 500 m in range of the UPC sensor's location and was oscillating due to the influence of the wind.

Figure 3 - 4 Left: Satellite photo of the Collserola test-site, in the outskirts of Barcelona. Right: Photo of the Collserola test-site observed from the UPC sensor's location

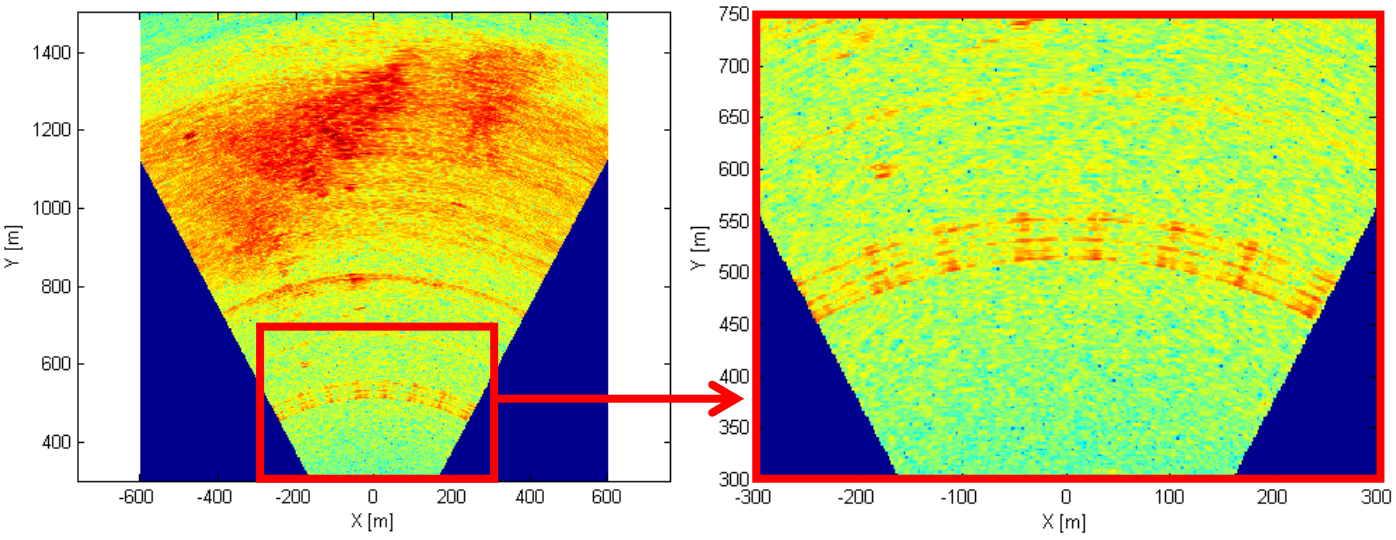

Figure 3 - 5 Left: Focused image of the Collserola test site. Right: Zoom on the crane

Figure 3 - 5 shows the same effect of the replicas simulated in Figure 3 - 3. In the Collserola test site measurement, replicas of the crane appear in all the radial range as expected. The oscillation period of the crane is unknown, but according to the previous simulations the movement is subsampled and because of that the effect of the replicas is observed in the focused image.

3.3.2 One dimensional simulations and measurements

In order to evaluate the behavior of the phase of an oscillating target, a set of one dimensional simulations and measurements have been performed. In a one dimensional simulation or measurement, the SAR system is not moving to perform a synthetic aperture. In this way, all the received echoes are from the same location of the transmitting and receiving antennas and the phase of the retrieved data does not need compensation relative to the movement of the SAR. The focused image of a one dimensional measurement is obtained with the same process that an image obtained realizing the synthetic aperture. Because of that, a focused image of a one dimensional measurement concentrates all the information of the measurement in the center of the image. Figure 3 - 6 shows an ideal simulated static target focalized applying the Fourier transform in range and in cross range. In this case, the target appears as a concentrated point in the focused image. To apply this focalization method, some assumptions have to be done. From the range Fourier transform in Equation 2.6 - 14 the pixel $P(x,y)$ of an image is obtained by

$$P(x,y) = \sum_{n=0}^{N} S_{cn}(\omega,u) e^{+j\beta t_n} e^{-j\alpha {t_n}^2}$$

Equation 3.3 - 1

where the terms $e^{+j\beta t_n}$ and $e^{-j\alpha {t_n}^2}$ are the RVP compensation and n are the cross range samples associated to the pixel (x,y). Working with a short aperture, the discrete summation of all the terms in cross range can be approximated by an integral in continuous time domain, which can be assumed to be equivalent to the Fourier transform in cross range.

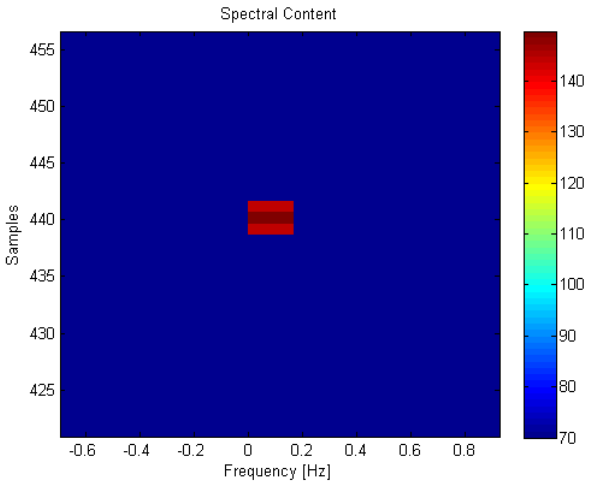

Figure 3 - 6 Focalization by the Fourier transform in cross range of a static target

In the following simulations and the measurements, the phase related to the target is going to be evaluated, as it depends of the distance from the SAR system to the target's location. Figure 3 - 7 shows the focused image of a target that varies its position oscillating 10 mm in the cross-range direction and the phase associated to that movement. It can be seen that an oscillation in cross range does not affect to the focusing of the target in the image, as the target appears as the static target focalized in Figure 3 - 6. During the six seconds of observation time, the phase cell 440 equivalent to the target present an oscillation of negligible amplitude ($4.5 \cdot 10^{-5}$mm).

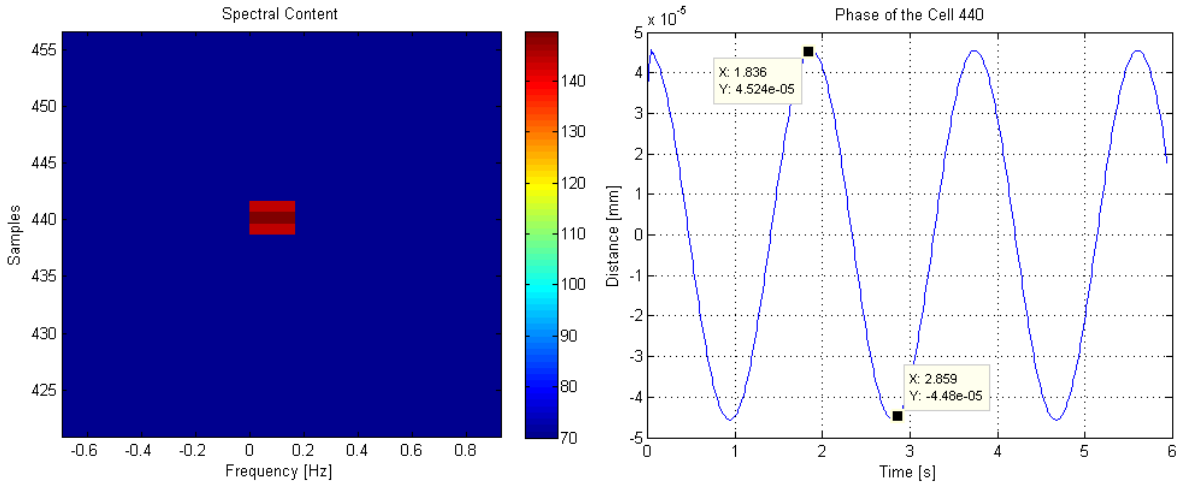

Figure 3 - 7 Left:Focalization of the target with an oscillation of 10mm in cross range. Right: Phase of the target

Figure 3 - 8 and Figure 3 - 9 show an oscillating target in the range direction with two different amplitudes: 10mm and 100mm. In both cases, the oscillation period is slower than in the case of Figure 3 - 7. Despite of this, comparing the oscillation in cross range with amplitude of 10mm with the oscillation in range of 10 mm it can be seen in the spectral content that for the second case the oscillation affects much more to the focused image. The spreading effect in the focused image is even more obvious when the amplitude of the oscillation is larger, as can be seen in the focused image for a target oscillating in range with amplitude of 100 mm.

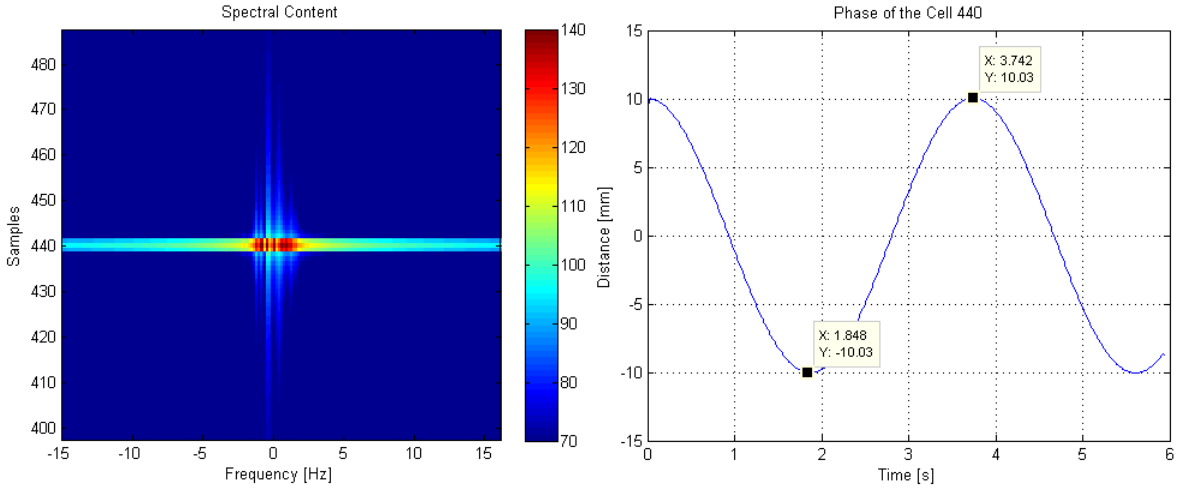

Figure 3 - 8 Left: Focalization of the target with an oscillation of 10mm in range. Right: Phase of the target.

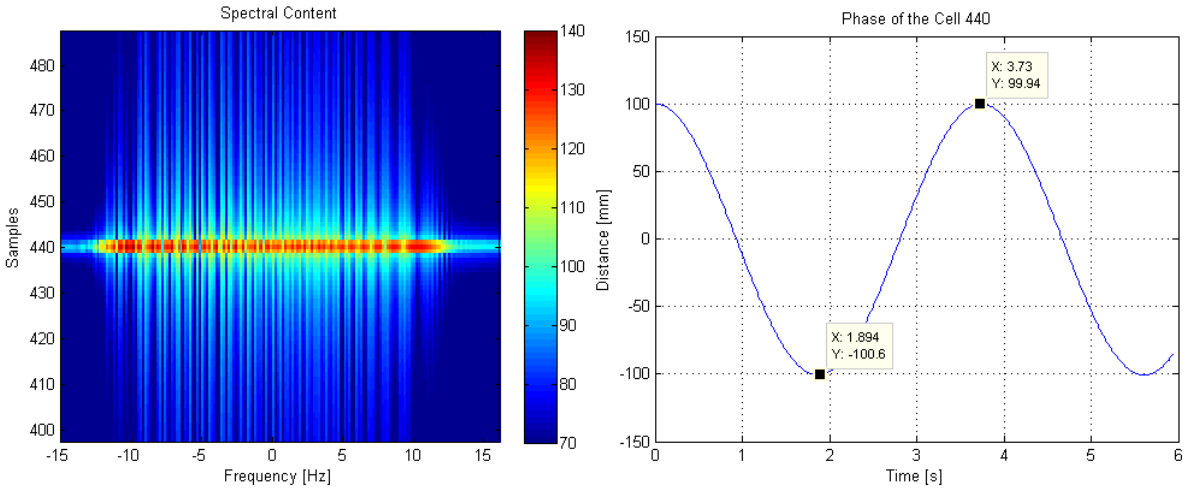

Figure 3 - 9 Left: Focalization of the target with an oscillation of 100mm in range. Right: Phase of the target

To validate the simulations, a one dimensional measurement of the Collserola test site has been performed. The scenario included a crane that was located in front of the UPC SAR system at a distance of approximately 500m. Figure 3 - 10 shows the focalized image and the phase of the sample related to the crane.

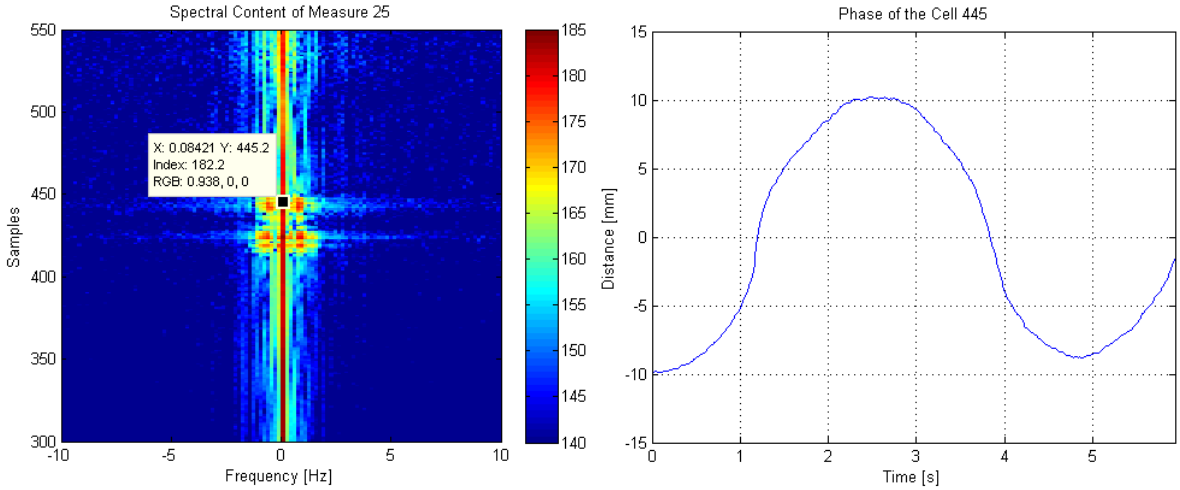

Figure 3 - 10 Left: Spectral content of the crane. Right: Retrieved phase of the cell related to the crane

The spreading of the spectral content in the focalized image in Figure 3 - 10 is obvious. Observing the phase related to the crane, a period of a sinusoid function can be seen. The sinusoid function reveals the oscillation of roughly 20mm of the crane in the range direction due to the effect of the wind.

3.3 W Band GBSAR Measurements

The purpose of this section is to detect little oscillations of a target using the W band UPC SAR operating at 94GHz. Regarding to the previous section, the effects in the phase of a moving target will be analyzed. As this radar operates at very high frequencies, very little displacements of an object have to show its impact on the phase of the measurement. The

stability of the system and the minimum displacement in range that this sensor is able to resolve will be analyzed.

3.3.1 Stability of the W band GBSAR system

The W band UPC sensor operates at a very high frequency, so little disturbances on the atmosphere such as a change of temperature or humidity can affect the measurements. To evaluate this impact, the W band sensor has been located in the UPC anechoic camber to make a sort of one dimensional measurements. Two trihedral corner reflectors have been located at a range distance of approximately 4.5 m and 7 m from the sensor. The sensor is programmed to perform 100 measures every 10 seconds (T1=16.6 minutes), then 100 more measures every 30 seconds (T2=50 minutes) and finally 150 measures every 300 seconds (T3=12.5 hours). Figure 3 - 11 shows the evolution of the phase of the two trihedral along the T1, T2 and T3 intervals of measurement.

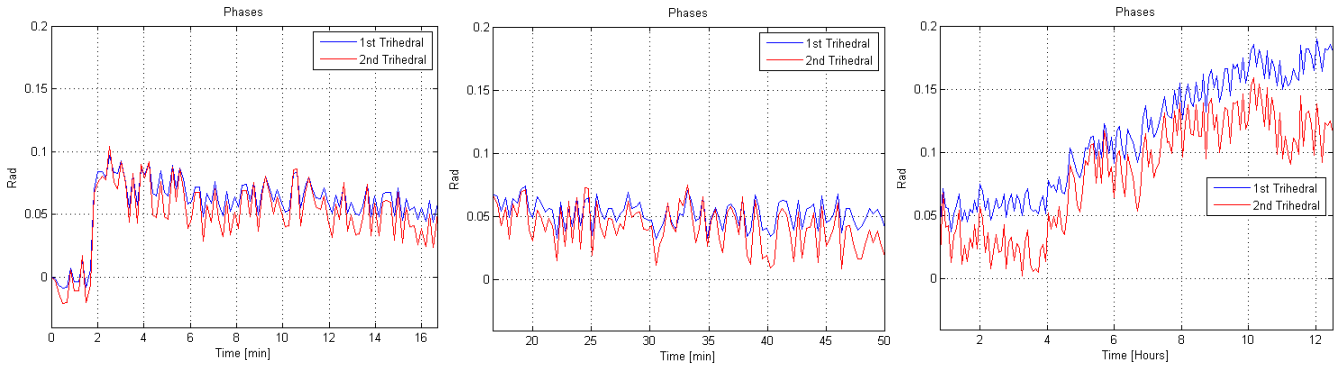

Figure 3 - 11 Left: Phase of the trihedral during T1 (16.6 min). Center: Phase of the trihedral during T2 (50 min). Right: Phase of the trihedral during T3 (12.5 h)

In Figure 3 - 11 it can be seen that the retrieved phase evolution of the two trihedral are the same and it is concluded that their evolution don't depend on the target and its location but on the sensor. During the two first minutes the system needs to be stabilized in temperature, which is traduced in an abrupt change of the phase of the targets (Figure 3 - 11 left). The fact that the sensor does not have a *Proportional Integral Derivative* (PID) temperature controller has to be taken into account. After the thermal stabilization of the system, the phase remains almost constant during the following five hours (Figure 3 - 11 center and right). As it was dawning, the temperature and conditions of the atmosphere in the anechoic chamber changed and the phase started to increase (Figure 3 - 11 right). It has to be taken into account that, due to changes in the temperature of the scenario, a phase drift of approximately 0.2 radians have been introduced.

3.3.2 W band GBSAR system positioning measurements

To evaluate the maximum increment in range that the W band GBSAR system is able to resolve through the analysis of the evolution of the phase, two experiments have been performed carrying out a set of one dimensional measurements. In both experiments, a trihedral has been located inside the UPC anechoic chamber at a certain distance in range from the radar. Said trihedral in turn has been mounted above a micrometric positioner in order to control the

increment of distance in every measure. In experiment 1, increments in range from 50µm to 400µm have been developed while in experiment 2 the increments are comprised between 5µm and 100µm. Table 3 - 1 and Table 3 - 2 show the relative range and the range increment for experiment 1 and experiment 2 respectively. The relative range is de displacement with respect to the range of the measure 1 and the range increment is the increment in range with respect to the previous measure. In both experiments the first measure is the reference one, the second measure is a redundant measure without any displacement and the third measure is a redundant measure without any displacement but entering in the anechoic chamber to analyze if some disturbance is created by only entering to move the trihedral.

	Meas 1	**Meas 2**	**Meas 3**	**Meas 4**	**Meas 5**	**Meas 6**	**Meas 7**	**Meas 8**	**Meas 9**	**Meas 10**
Relative Range[µm]	0	0	0	50	100	200	500	800	1200	1600
Range increment[µm]	-	0	0	50	50	100	300	300	400	400

Table 3 - 1 Relative range and range increment between measurements in experiment 1

	Meas 1	**Meas 2**	**Meas 3**	**Meas 4**	**Meas 5**	**Meas 6**	**Meas 7**	**Meas 8**	**Meas 9**	**Meas 10**	**Meas 11**	**Meas 12**	**Meas 13**
Relative Range[µm]	0	0	0	5	10	15	20	30	40	50	70	100	200
Range increment[µm]	-	0	0	5	5	5	5	10	10	10	20	30	100

Table 3 - 2 Relative range and range increment between measurements in experiment 2

Figure 3 - 12 shows the comparison between the theoretical range and the measured range and the error between the theoretical range and the measured one for the experiment 1 and 2.

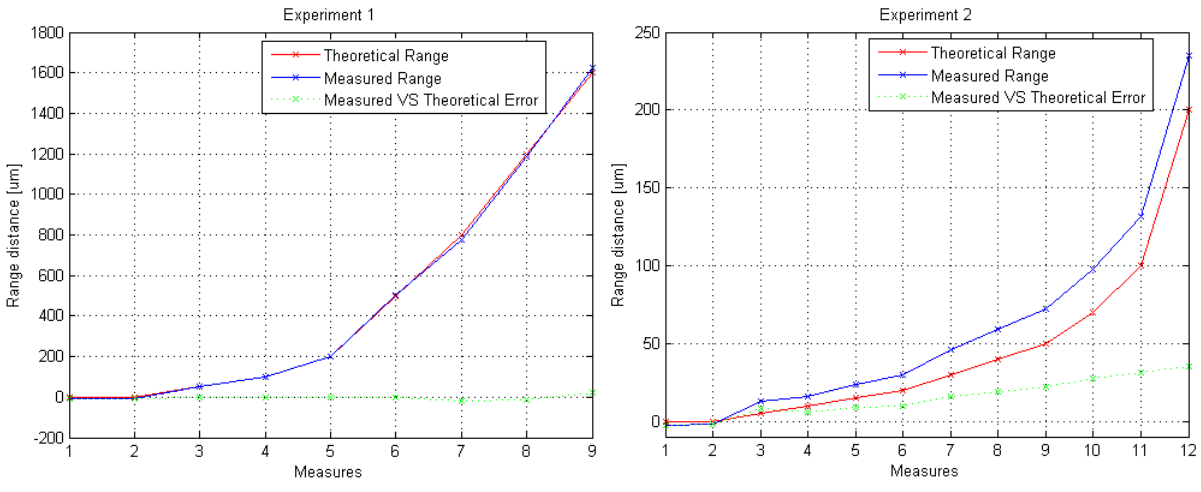

Figure 3 - 12 Left: Range measurements for experiment 1. Right: Range measurements for experiment 2.

In Figure 3 - 12 left can be observed that for range increments of 50µm onwards the theoretical range and the measured one are almost the same. Thereby, for experiment 1 the error between the measured and the theoretical range is nearly 0. In the case of experiment 2, Figure 3 - 12 right shows slightly differences between the measured and the theoretical range. Aversely, the measured curve and the theoretical one follow the same shape. So the error is introduced when displacing the trihedral with the micrometric positioner, since is so difficult to displace 5µm accurately by hand. It can be concluded that with the W band UPC GBSAR, displacements in range of 5 µm can be detected.

3.3.3 Measurement of oscillating targets with W band GBSAR system

In order to analyze the oscillation of a punctual target in a controlled environment with the W band GBSAR, the experiment of **Figure 3 - 13** left has been developed. In this experiment, two targets are located at approximately 4.4 m and 5.6 m in range from the radar (**Figure 3 - 13** right); a trihedral and an oscillating target. The oscillating target is implemented by sticking a flat surface with reflective material to the membrane of a speaker. When a sinusoid function of a determined frequency and amplitude is introduced to the speaker, its membrane oscillates and so does the flat surface adhered on it.

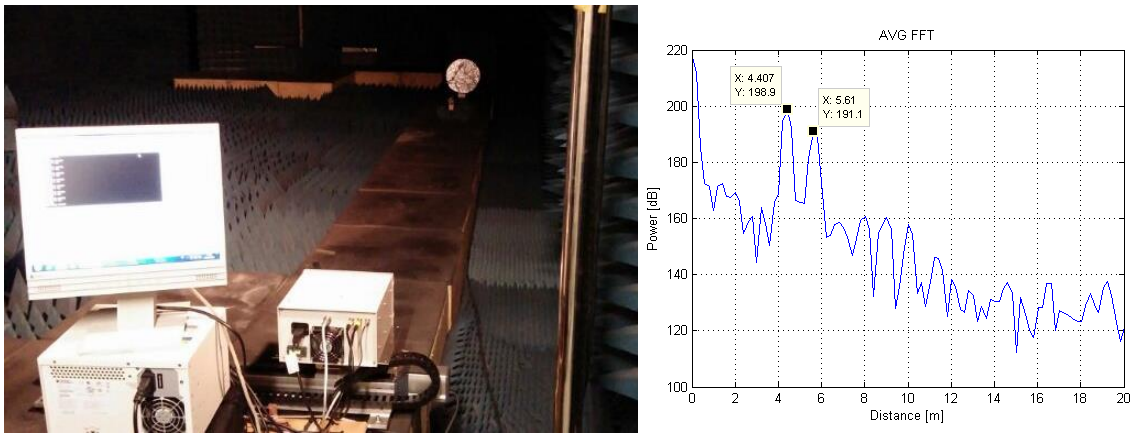

Figure 3 - 13 Left: Measuring an oscillating target in the UPC anechoic chamber with the W band GBSAR. Right: Distance from the radar to the targets. Trihedral at 4.4m and oscillating target at 5.6m

A set of one dimensional measurements have been performed to analyze the evolution of the phase of an oscillating target (Figure 3 - 14). Sinusoid functions of 5HZ and 10Hz with amplitudes of 1V and 3V have been introduced to the speaker. Figure 3 - 14 shows the measurement of the phase of the oscillating target for these amplitudes and frequencies. It can be seen that the recovered phase follows the sinusoid function introduced to the speaker. The period of the recovered phase is 5Hz and 10Hz as expected and its amplitude is higher with 3V than in the case of 1V, due to a major displacement of the membrane of the speaker for higher amplitudes.

After analyzing the evolution of the phase in one dimensional measurements, a synthetic aperture is performed with the same distribution of the system showed in Figure 3 - 13 left, in order to analyze the impact of the oscillating target in the focused image. Three different oscillating periods of the sinusoid function introduced to the speaker have been contemplated;

50mHz, 100mHz and 500mHz. For the three cases, the input amplitude is 5V. Figure 3 - 15 shows the focalized image for the three cases.

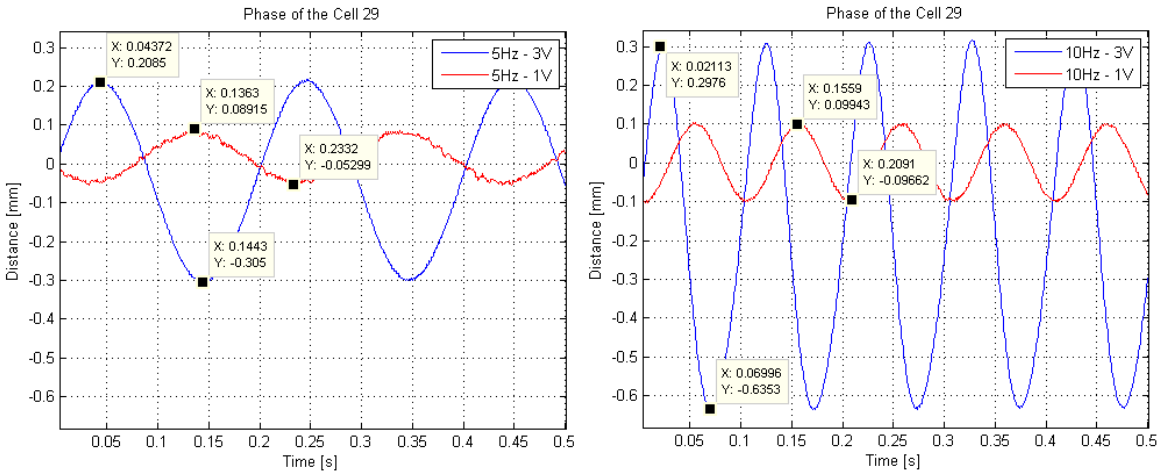

Figure 3 - 14 Phase of the oscillating target

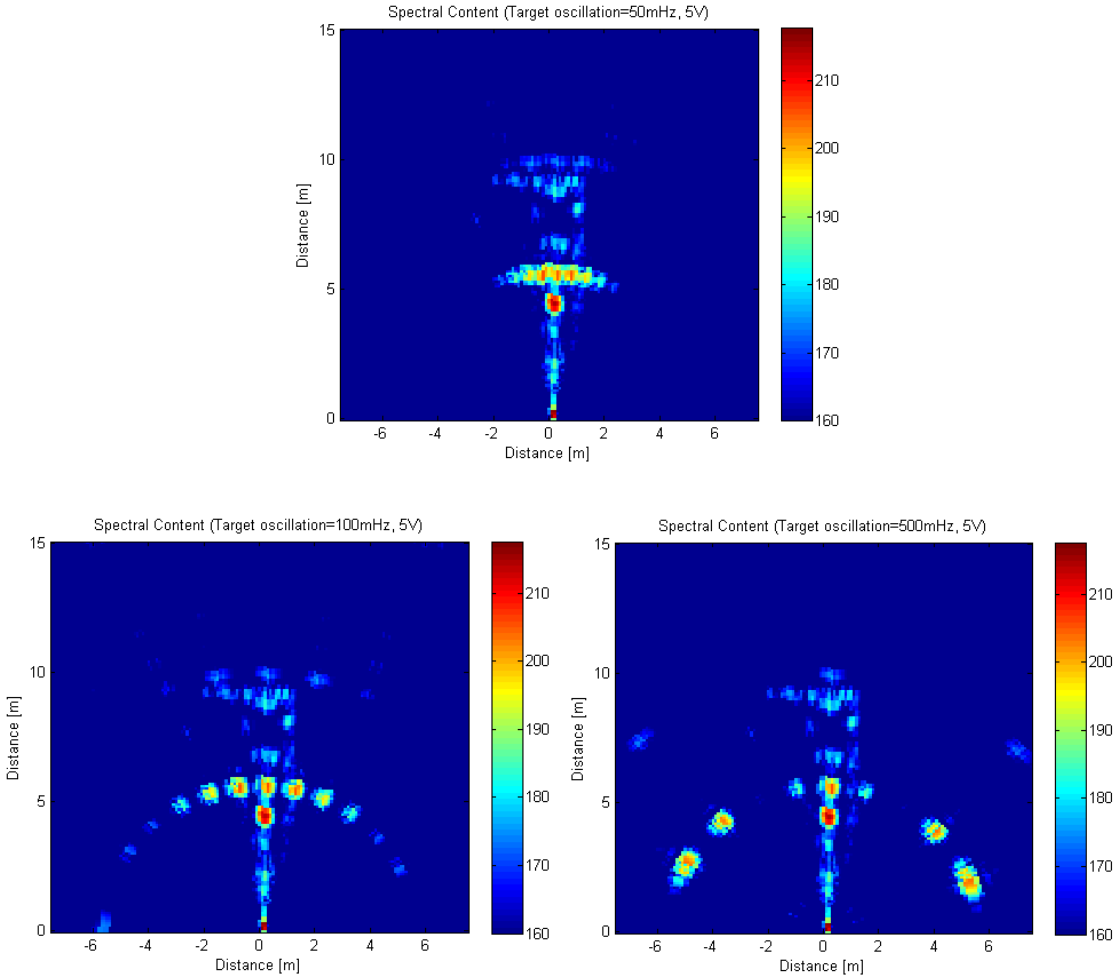

Figure 3 - 15 Focused image of oscillating target. Top: 50 mHz period, 5 V amplitude. Bottom left: 100 mHz period, 5 V amplitude. Bottom right: 500 mHz period, 5 V amplitude.

In the images of the Figure 3 - 15 it can be seen the trihedral located at a distance of 4.4m and the speaker at a distance of 5.6m. For the speaker oscillating at a frequency of 50mHz (Figure 3

- 15 top), the focused image reveals an spreading in cross range of the target. As the speaker oscillates at higher frequencies (Figure 3 - 15 bottom left and bottom right), it results in a higher spreading of the target in cross range up to the point to start appearing some replicas for the same radial range location. These results are consistent with the simulations of section 3.3.1.

To better visualize the spreading in the cross range spectrum of an oscillating target, Figure 3 - 16 shows a comparison between the measured cross range spectrum of the trihedral and the measured cross range spectrum of the speaker oscillating at 50 mHz with an input amplitude of 5V.

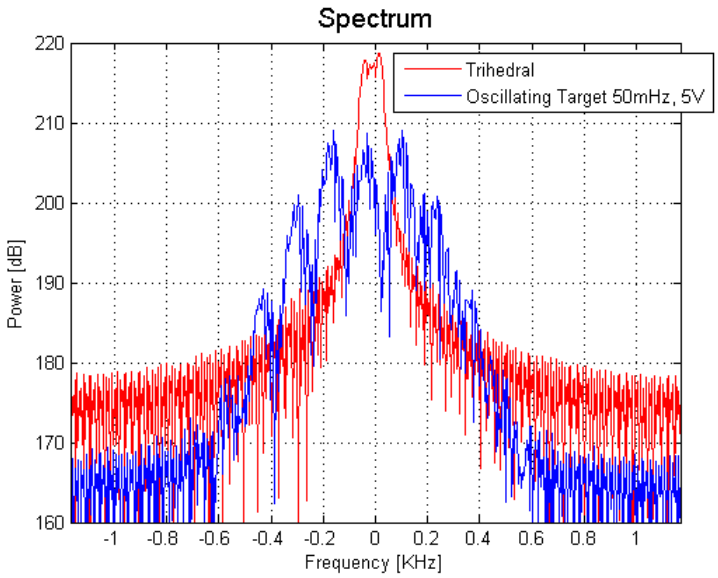

Figure 3 - 16 Comparison of the spectrum of the trihedral and the speaker oscillating at 50 mHz with an input amplitude of 5V

By comparing both spectrums in Figure 3 - 16, the spreading of the oscillating target is easily observable.

Windblown Radar Ground Clutter and its influence in the focused image

4.1 Introduction to windblown radar ground clutter

Ground clutter is a form of radar signal contamination and is also called ground return, surface clutter, land clutter or terrain clutter. Radar returns are produced from nearly all surfaces when illuminated by a radar. Such echoes are typically returned from ground, sea, rain, animals/insects, atmospheric turbulences and can cause serious performance issues with radar systems.

Windblown ground clutter is a different phenomenon related with the scintillation of vegetation. This effect can be explained analogously with a photographic camera. Is the equivalent of a scene being photographed with a camera in which some elements are in movement. If the shutter time is slow with respect to the movement of the elements, the picture will appear blurred. Something similar happens in the case of a SAR illuminating an scene with vegetated areas. Due to the effect of the wind, vegetation moves randomly while realizing the measure and this is translated in a blurring effect of the focused image in the cross range direction. As in the case of a photographic camera, the longest the observation time, the higher the blurring effect in the focused image.

The present chapter is focused on the study of windblown radar ground clutter by means of some simulations together with experimental measurements with the X-band UPC GBSAR.

4.2 Model for the Doppler Spectrum of Windblown Radar Ground Clutter

The power-law spectral model has been widely used for a number of years to represent Doppler spectra due to intrinsic motion in radar ground clutter. The model was shown to provide a good fit to experimentally measured clutter echo signatures under a number of different conditions. However, these previous measurements were taken with limited dynamic ranges (up to 35-40 dB) due to technological limitations. Extensive measurement campaigns with a dynamic range of 80 dB revealed that the measured ground clutter spectra are often approximated by an exponential shape. It is therefore of interest to investigate whether a theoretical interpretation is available for an exponential shape of the power spectral density

(PSD). The purpose of this section is to derive a model for the PSD of windblown vegetation over a wide dynamic range. The derived model will be compared to measured spectra to assess its validity. The ability of the model to fit the quasi-dc region of the clutter spectrum is also analyzed.

4.2.1 Quasi-DC component and K-PSD model

In [Billingsley ,87] and [Billingsley ,96], to achieve a reasonable fit of the measured spectra, the quasi-dc spectral power was included in a dc Dirac delta term. This is justified theoretically by assuming the probability of having a static scatterer to be r times higher than the probability of having a dynamic scatterer following the multiscale motion model [Billingsley , 99].

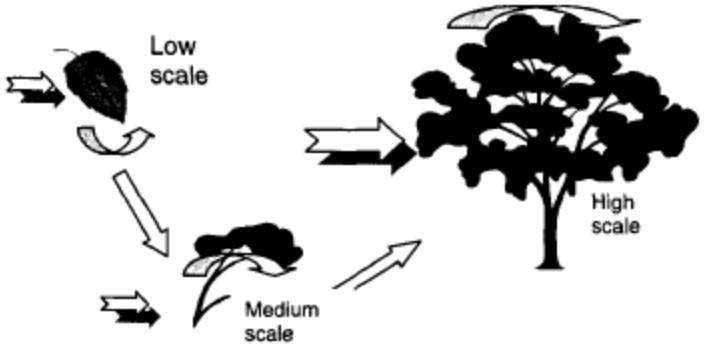

Figure 4 - 1 Multiscale model for windblown vegetation

The distribution of the number of velocity components N in this case is

$$P_N(N) = \frac{r}{1+r}\delta(N) + \frac{1}{1+r}\binom{N+\alpha+1}{\alpha-1}\frac{(\bar{N}/\alpha)^N}{(1+\bar{N}/\alpha)^{N+\alpha}} \qquad \textbf{Equation 4.2 - 1}$$

The total clutter power is divided between the dc spike and the ac spectrum, according to the probabilities of the two events, as

$$P(v) = \frac{1}{1+r}\frac{\beta}{2}e^{-\beta|v|} + \frac{r}{1+r}\delta(v) \qquad \textbf{Equation 4.2 - 2}$$

where v is the Doppler velocity in m/s, r is the ratio of dc power to ac power in the spectrum, $\delta(v)$ is the Dirac delta function, which properly represents the shape of the dc component in the spectrum, and $\frac{\beta}{2}e^{-\beta|v|}$ represents the shape of the ac component of the spectrum ($P_{ac}(v)$). In the ac component of the spectrum, β is the exponential shape parameter. Equation 4.2 - 2 encodes the assumption that with probability $r/(1+r)$ the radar pulse is backscattered by a static reflector (ground, main tree trunk, etc.), and with probability $1/(1+r)$ it is backscattered by the windblown foliage.

Figure 4 - 2 provides values of β as a function of wind conditions such that the spectral width increases with increasing wind speed as generally observed in the measurement data. The

measurements indicate that the values of β in Figure 4 - 2 are largely independent for radar carrier frequency over the range from VHF to X band.

Wind Conditions	Wind Speed (mph)	Exponential ac Shape Parameter β $(m/s)^{-1}$	
		Typical	Worst Case
Light air	1-7	12	—
Breezy	7-15	8	—
Windy	15-30	5.7	5.2
Gale force (est.)	30-60	4.3	3.8

Figure 4 - 2 Exponential ac shape parameter **β** vs wind speed

An algebraic expression for β that incorporates linear dependency of spectral width on the logarithm of the wind speed as observed in measured data is

$$\beta^{-1} = 0.1048[log_{10}w + 0.4147] \qquad \textbf{Equation 4.2 - 3}$$

where w is wind speed in statute miles per hour.

Although $P_{ac}(v)$ is largely independent of radar frequency, the value of the dc/ac ratio r in Equation 4.2 - 2 is strongly dependent on both wind speed and radar frequency. An analytic expression for r empirically derived from some results which generally capture these dependencies is provided by

$$r = 489.8w^{-1.55}f_0^{-1.21} \qquad \textbf{Equation 4.2 - 4}$$

where, as before, w is the wind speed in statute miles per hour, and f_0 is the radar carrier frequency. Equation 4.2 - 4 applies to cells containing windblown trees. The database from which it was derived covers the frequency range from VHF to X Band and includes measurements from many forested cells under various wind conditions.

The general expression for the clutter spectrum called K-PSD is

$$P(v) = \frac{\beta}{\sqrt{\pi}\Gamma(\alpha)}\left(\frac{\beta}{2}|v|\right)^{\alpha-\frac{1}{2}} K_{\alpha-\frac{1}{2}}(\beta|v|) \qquad \textbf{Equation 4.2 - 5}$$

where K_ξ is the modified Bessel function of the second type and order ξ. Observe that, for large values of $|v|$, the K-PSD functions in Equation 4.2 - 5 have an asymptotic behavior as

$$P_{\infty}(v) = \frac{\beta}{2\Gamma(\alpha)}\left(\frac{\beta}{2}|v|\right)^{\alpha-1} e^{-\beta|v|}$$

Equation 4.2 - 6

Thus, for large $|v|$ the negative exponential shape is dominant, so that the slope of the decay becomes essentially exponential. The value of the parameter α controls the scaling of the exponential slope and the shape of the peak at dc. Moreover, α also controls the global variance of the clutter PSD, since this is given by $\sigma_v^2 = 2\alpha/\beta^2$.

The K-PSD model is highly appropriate for characterizing clutter spectra from purely windblown vegetation, where even the slowest motion components are assumed to have nonzero spectral width.

4.3 X Band GBSAR measurements

In order to characterize the influence of the vegetation in the focused images and to evaluate the validity of the K-PSD model, some measurements with the X band UPC GBSAR have been developed.

4.3.1 One dimensional measurements

A set of forty seven acquisitions in 24 hours in the Collserola range test site have been performed, all of them as one dimensional measurements. In such measurements, two parabolic antennas with high directivity have been used, as can be seen in Figure 4 - 3. The two antennas are pointing to a vegetated area mainly composed of pine trees.

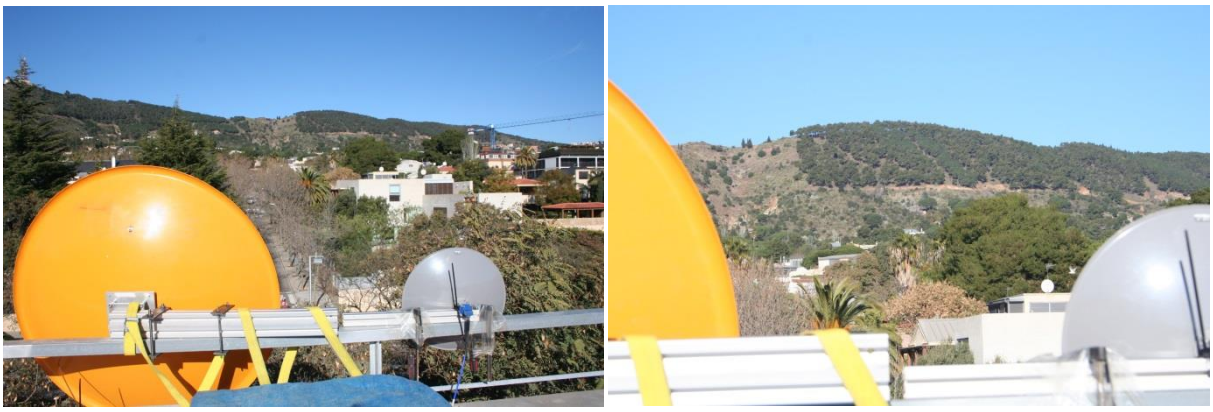

Figure 4 - 3 Left: Location of the parabolic antennas in the Collserola test site. Rigth: Zoom to the vegetated area illuminated.

As the aim of the experiment is to correlate the intensity of the wind and the blurring effect in the measured images due to the scintillation of the vegetation, the velocity of the wind at the moment of the measurements needs to be known. In this measurement campaign, the velocity of the wind has been estimated taking its value from the data provided by the Servei Meteorològic de Catalunya from the closest meteorological weather station.

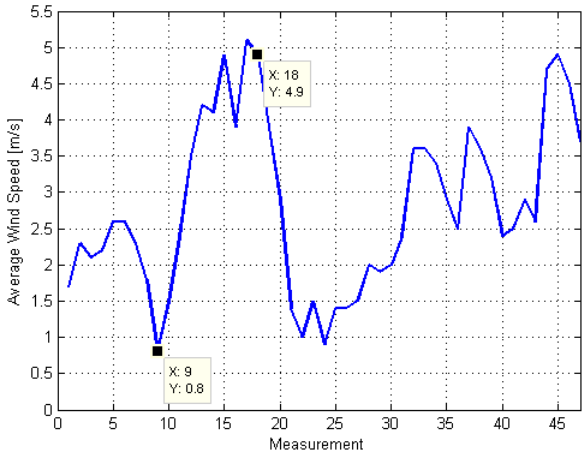

Figure 4 - 4 Average wind speed provided by the Serveimeteorològic de Catalunya

Figure 4 - 4 depicts the evolution of the average wind speed during the measurement period. Measurement 9, performed at 22:22 h, is the one in which the average wind speed is minimum with a velocity of 0.8 m/s. On the contrary, measurement 18 at 2:55 h is one with the highest average velocities with a value of 4.9 m/s. Figure 4 - 5 shows the focalized image of the measurements 9 and 18 applying the method of the Fourier transform in range and in cross range explained in the previous chapter.

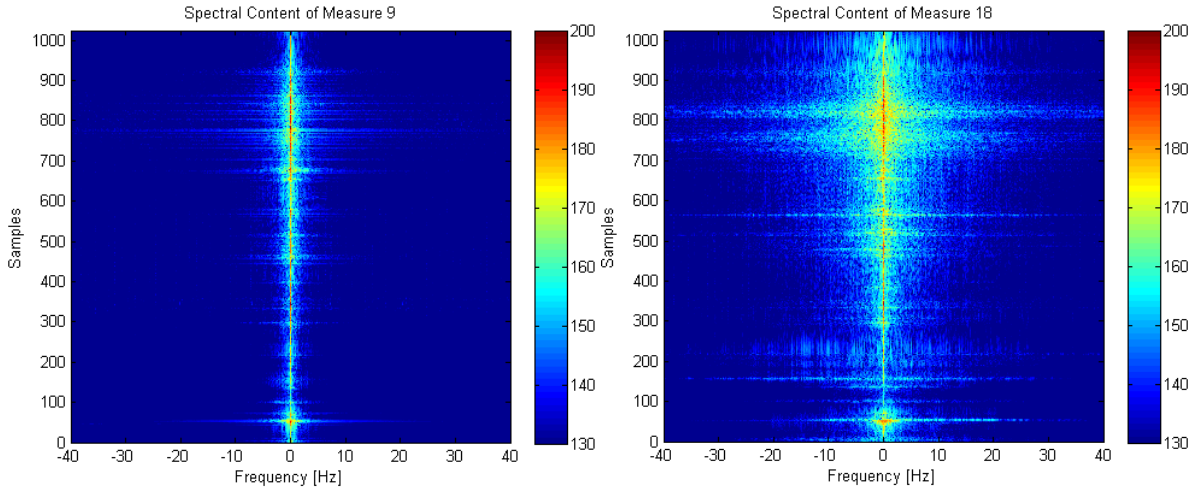

Figure 4 - 5 Left: Spectral content of measure 9 with average wind velocity of 0.8 m/s. Right: Spectral content of measure 18with average wind velocity of 4.9 m/s

Comparing the spectral content of measure 9 and measure 18, the effect of the wind it is easily observable. Due to the scintillation of the vegetation produced by the wind, the blurring effect in the focused image is much more evident in measurement 18 than in measurement 9.

To analyze the effect of the wind over the cross range spectrum, the power spectral density (PSD) of a cell corresponding to an static target and of a cell corresponding to the vegetated area has been computed. Figure 4 - 6 shows the PSD of the cell 346 (static target) and 800 (vegetated area) for two different average wind speed; 1.8 m/s and 3.9 m/s.

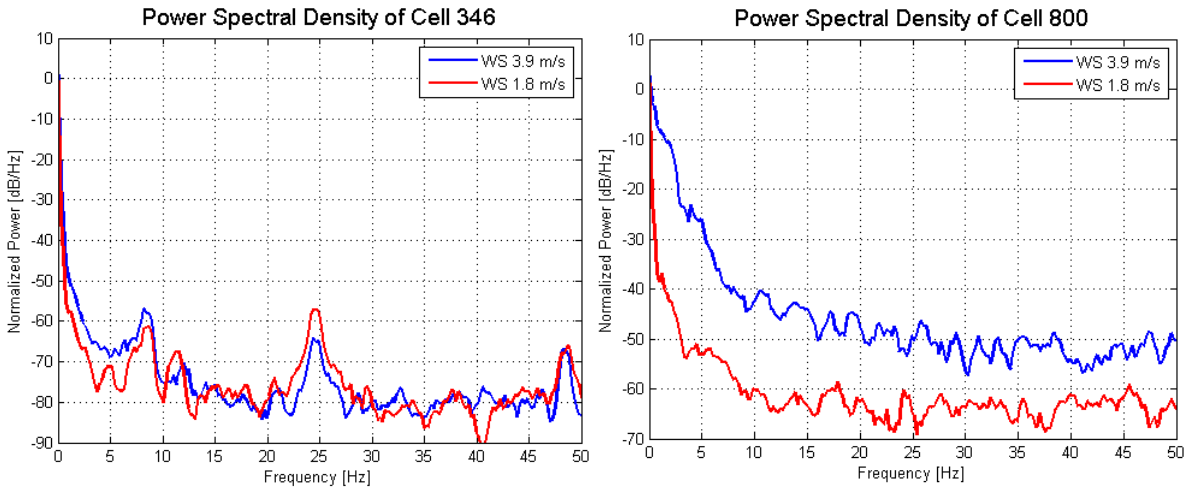

Figure 4 - 6 Left: PSD of cell 346 (static target) for wind speeds of 1.8 m/s and 3.9 m/s. Right: PSD of cell 800 (vegetated area) for wind speeds of 1.8 m/s and 3.9 m/s.

As can be seen in Figure 4 - 6, the PSD corresponding to the vegetated area suffers an important spreading with the increase of the average wind speed, while the PSD corresponding to an static target remains almost constant. In the case of the static target, the little spreading in low Doppler frequencies is probably produced for the vegetated areas in the adjacent pixels. Figure 4 - 7 compares the PSD of measure 9 and 18 for the cell 346 and 800, superimposed to the theoretical exponential shape of the K-PSD model for windblown ground clutter.

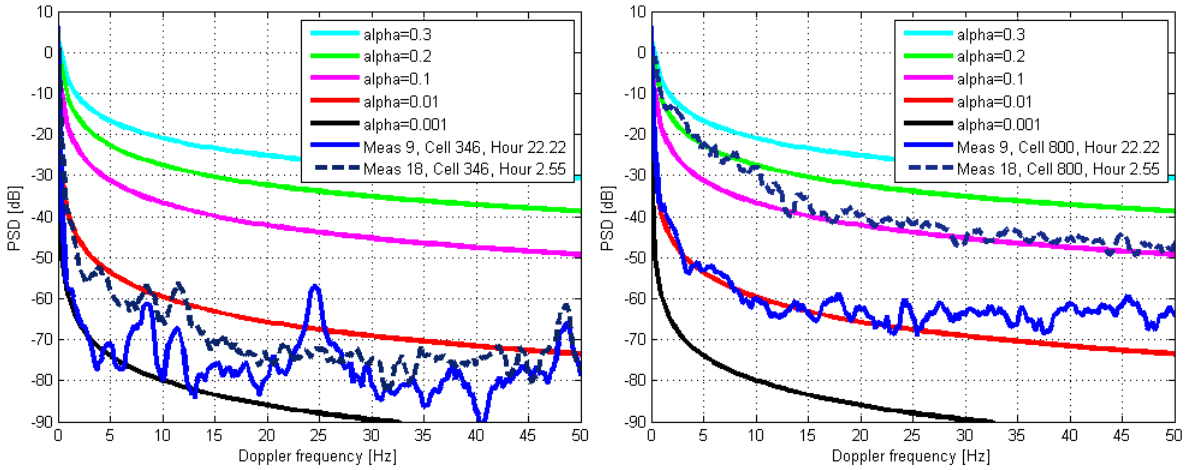

Figure 4 - 7 Left: K-PSD simulation and comparison of cell 346 (static target) for measurement 9 and 18. Right: K-PSD simulation and comparison of cell 800 (vegetated area) for measurement 9 and 18.

In Figure 4 - 7 the K-PSD model has been simulated for different values of $\alpha < 1$, which concentrates large power contributions near dc. The first important result is that the measured PSD fits the exponential shape of the K-PSD model. Comparing the PSD of measure 9 and 18 for the cell 346 (Figure 4 - 7 left), can be seen that even being an static target the PSD of the measure with high wind speed suffers a little spreading, due to the contamination of adjacent cells. The PSD of the cell 346 corresponding to the measure 9 fits perfectly the K-PSD model with $\alpha = 0.001$, while the PSD of measure 18 is between $0.001 < \alpha < 0.01$. In the

case of the cell 800 corresponding to vegetated area, the PSD for measurement 9 and 18 are too different. The PSD of measure 9 fits perfectly the K-PSD model for $\alpha = 0.01$, while the PSD of measure 18 follows the K-PSD model for a value of alpha between $0.1 < \alpha < 0.2$. In this case, is evident that the faster the wind speed in the vegetated area, the larger the spreading of the spectrum due to the scintillation of the vegetation. Finally, comparing the same measurement for the two different cells (static target and vegetated area), it can be seen that even with the presence of low wind speeds the spectrum of the vegetated area tends to be spread compared with the spectrum of the static target. For the case of intense wind (measurement 18), the measured spectrum of the static target (cell 346) and the vegetated area (cell 800) is far different.

A new experiment has been developed in the same scenario of Figure 3 - 4in the Collserola test site. The objective of such experiment is to corroborate the results obtained in the experiment explained before and to observe the relationship between the observation time of an acquisition and the blurring effect in the image.

Figure 4 - 8 shows the spectral content of measurement 25 and 37, which has the same observation time of 5.94 seconds, and the comparison of the K-PSD model with the PSD of the cell 957 for the two measurements. Measurement 25 was acquired at 10:57 h with low wind speed and measurement 37 was acquired at 16:07 h with high wind speed.

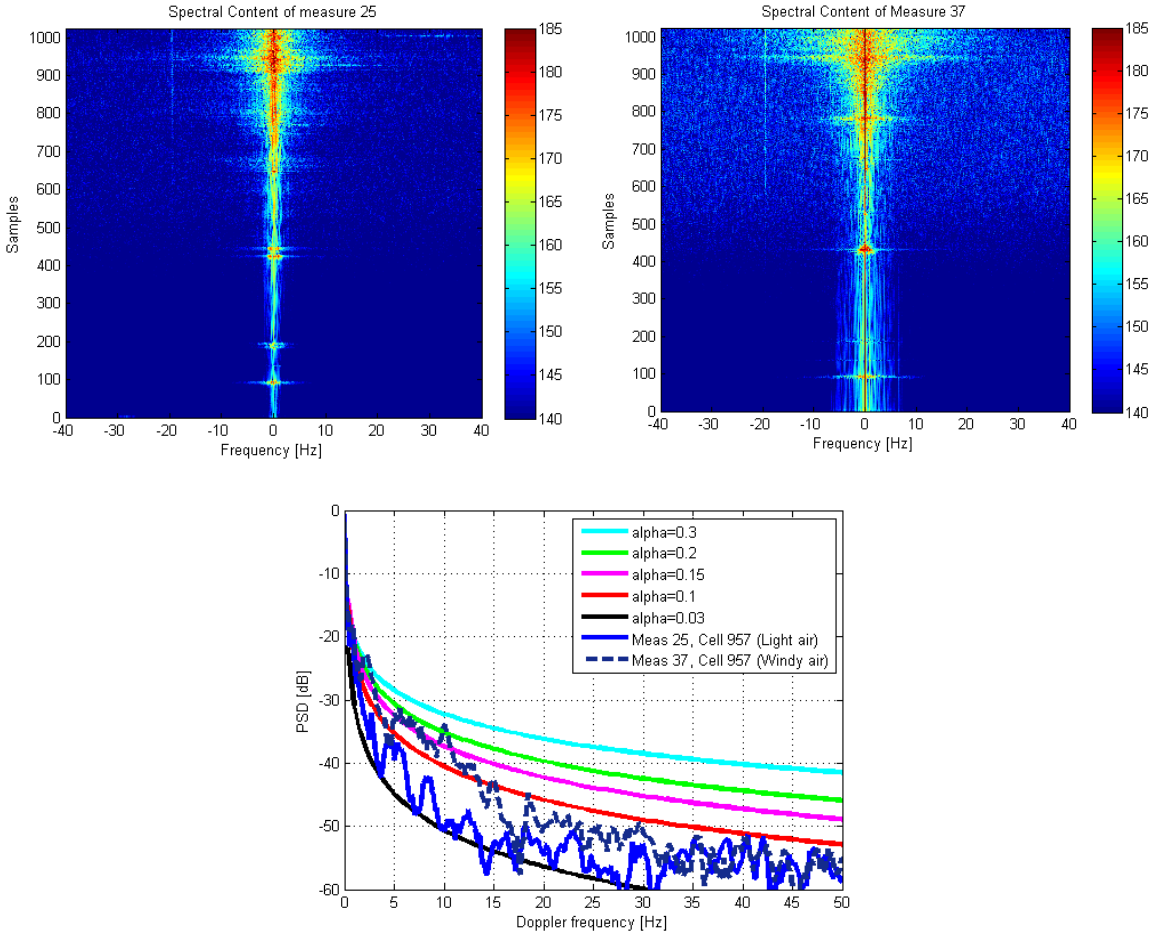

Figure 4 - 8 Top left: Spectral content of measure 25 (observation time of 5.94 seconds and low wind speed). Top right: Spectral content of measure 37 (observation time of 5.94 seconds and fast wind speed). Bottom: K-PSD simulation and comparison of cell 957 for measurement 25 and 37.

Comparing the spectral content of measure 25 and 37, the effect of the wind in the focused image is clear. This result is consistent with the previous experiment.

To compare the effect in the image of the scintillation of the vegetation with the observation time, a new measurement has been realized. Measurement 36 is done few minutes before measurement 37, assuring similar wind conditions in the same scenario. The only difference between measure 36 and 37 is the observation time, which is 11.89 seconds and 5.94 seconds respectively.

Figure 4 - 9 shows the spectral content of measure 36 and 37 and the comparison of the K-PSD model with the PSD of the cell 957 for the two measurements.

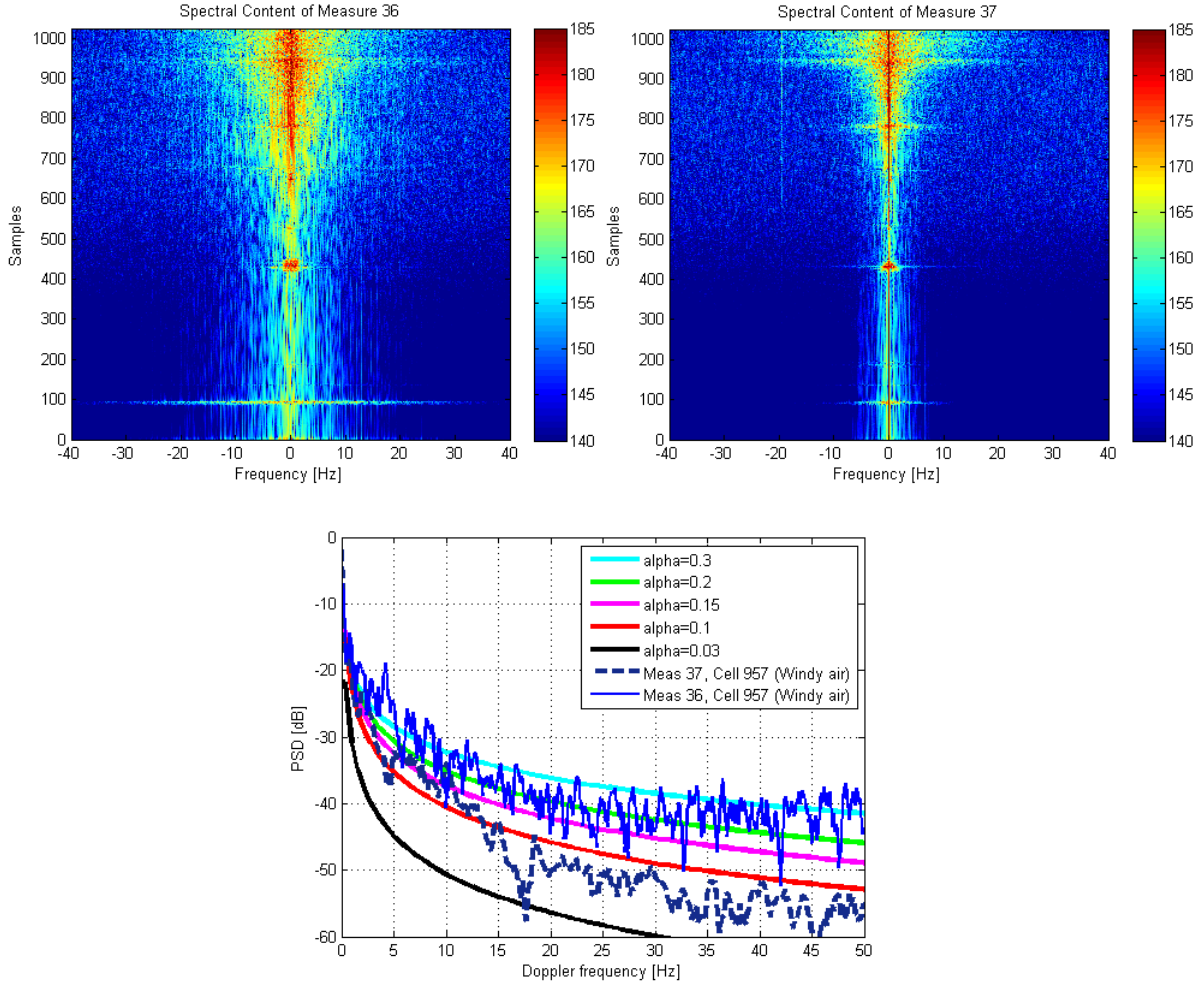

Figure 4 - 9 Top **l**eft: Spectral content of measure 36 (observation time of 11.89 seconds and fast wind speed). Top right: Spectral content of measure 37 (observation time of 5.94 seconds and fast wind speed). Bottom: K-PSD simulation and comparison of cell 957 for measurement 36 and 37.

Comparing measurements 36 and 37 it can be seen that for similar wind conditions and the same scenario, the observation time is an important parameter to ensure good quality in the focused image. The longer the observation time, the more evident is the spreading effect in the cross range spectrum.

4.3.2 Stop & Go vs FAST acquisitions

After having demonstrated the relation between the observation time and the blurring effect in the focused images, the effect in the images of two different working modes for the GBSAR is analyzed in this section. The Stop & Go mode divides the 2 meters synthetic aperture into 200 positions. In each antenna position, the system averages and stores 128 up ramp chirp signal to fill the raw data matrix. This method takes roughly 2 minutes to make one acquisition. The second method, called FAST, realizes the measure while the sensor is moving along the synthetic aperture, taking advantage of the slow time concept. The slow time concept states that as the radar signal propagates at the speed of light, the displacement of the SAR system during the forward and backward travel of the signal is negligible. The FAST acquisition method takes 4.3 seconds, which is a reduction in time with respect to the Stop & Go method of the 96.41%.

A new measurement campaign has been carried out in the emblematic mountain of Montserrat on July 23th 2014 with the X-band UPC GBSAR system. Figure 4 - 10 shows the location of the sensor in the geographical area of the Montserrat test site.

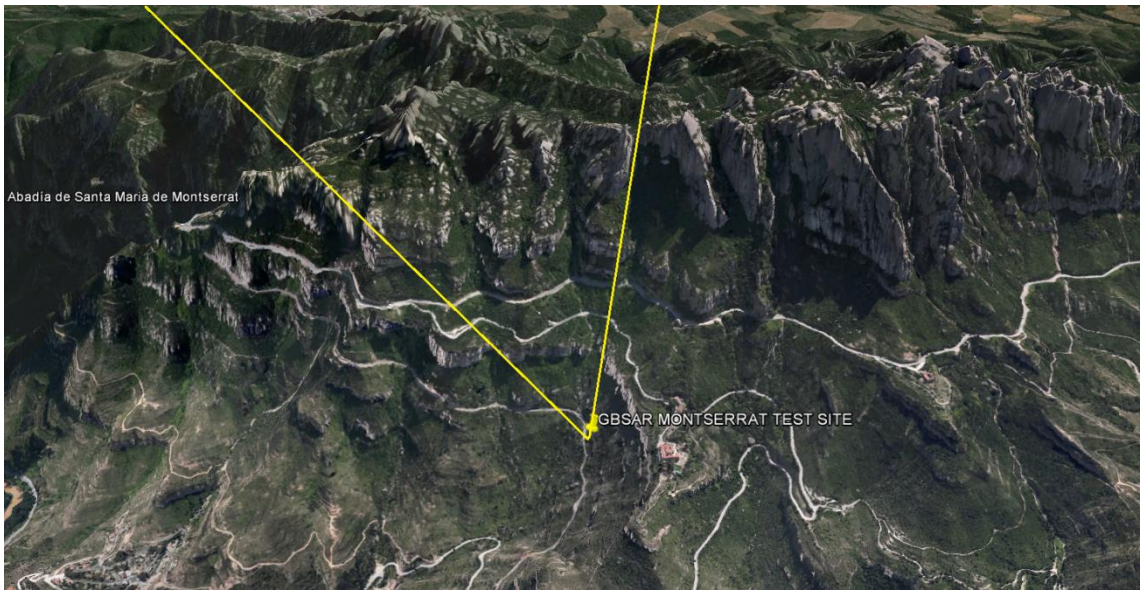

Figure 4 - 10 Location of the X band UPC GBSAR system in the Montserrat test site

Figure 4 - 11 left shows the X-band sensor mounted in the Montserrat test site and Figure 4 - 11 right shows the illuminated scene by the radar.

Figure 4 - 11 Left: X-band UPC GBSAR system mounted in the Montserrat test site. Right: Illuminated scene in the Montserrat test site.

Considering the illuminated area by the radar (Figure 4 - 11 right), it is easily observable that it is composed by vegetated areas and stone cliffs (composed by stone cliffs surrounded by dense vegetated areas). Consistently with the results obtained in previous sections of the present work, the vegetated areas should introduce the blurring effect in the cross range direction. To observe this phenomenon, two different measurements have been performed. The time between the two measurements is 4 minutes, so the wind conditions can be considered to be the same. The first measurement was at 12:24 h with the FAST mode and the second one was realized at 12:28 h with the Stop & Go mode. Figure 4 - 12 shows the focused image obtained with the X-band UPC SAR system transmitting and receiving with vertical polarization for the Stop & Go and FAST modes.

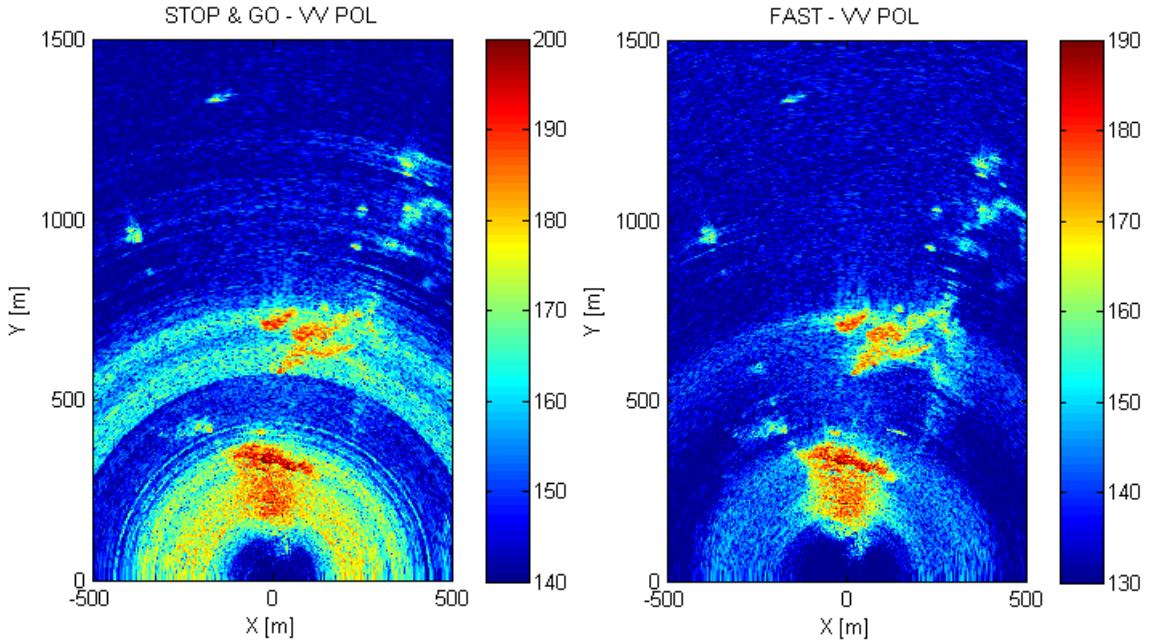

Figure 4 - 12 Left: X-Band UPC SAR system VV polarization focused image with Stop & Go mode. Right: X-Band UPC SAR system VV polarization focused image with FAST mode.

The first comment on the images of Figure 4 - 12 must be referred to the color bar axis. The limits of the Stop & Go measurement are higher than the ones of the FAST measurement. This

is due to the averaging process that takes part in the implementation of this mode of work. However, in both cases the dynamic range of the measure is the same; 60 dB's. Comparing the two images of Figure 4 - 12, it is evident that the blurring effect is much more noticeable in the case of Stop & Go measurement than in the case of the FAST measurement. Relating Figure 4 - 12 with the illuminated scene in Figure 4 - 11 right, it can be seen that the vegetated areas are the ones that produce said effect.

Up to this point, a deeper analysis of the effect of spectral resolution can be done. The spectral model in Equation 4.2 - 5 shows an infinite power level at dc for $\alpha < 1$. This agrees with the usual assumption of the presence of a spike at dc, which implies a Dirac delta function for $f_D = 0$. In the practical case of clutter spectral measurements, the frequency resolution is limited by the length of the measurement and by the spectral tapering used to suppress sidelobes. Therefore, in the analysis of measured radar clutter data, the spike component is masked by the convolution with the impulse response of the frequency analysis scheme. In order to compare the K-PSD spectral model with the spectra of measured data, a closed form expression is now derived which takes this convolution into account. If it is assumed that the sidelobes have been sufficiently reduced so that they do not affect the global shape of the spectrum, only the effect of the finite resolution needs to be considered. For simplicity, the impulse response is replaced with a rectangular shaped function of equal area, as

$$h(v) = \begin{cases} 1/(2\delta), & |v| < \delta \\ 0, & elsewhere \end{cases} \qquad \textbf{Equation 4.3 - 1}$$

where 2δ is the equivalent resolution. Recall the identity

$$D[x] = \int_0^x S(v)dv = \frac{1}{2\alpha\sqrt{\pi}\Gamma(\alpha)} \cdot$$

$$\left\{\alpha\beta\Gamma\left(\alpha-\frac{1}{2}\right)\ {}_1F_2\left[\frac{1}{2};\frac{1}{2},\frac{3}{2}-\alpha;\left(\frac{\beta}{2}x\right)^2\right] + \left(\frac{\beta}{2}x\right)^{2\alpha}\Gamma\left(\frac{1}{2}-\alpha\right)\ {}_1F_2\left[\alpha;\alpha+\frac{1}{2},\alpha+1;\left(\frac{\beta}{2}x\right)^2\right]\right\} \qquad \textbf{Equation 4.3 - 2}$$

where Γ is the Gamma function and ${}_1\mathrm{F}_2$is the generalized Hypergeometric function of order (1,2). Using this result, the convolution between Equation 4.2 - 5 and Equation 4.3 - 1 yields the effective spectral shape $\mathrm{S_e(v)}$, as

$$S_e(v) = \frac{1}{2\delta}\int_{v-\delta}^{v+\delta} S(v)dv = \frac{1}{2\delta}\begin{cases} D[|v+\delta|] - D[|v-\delta|], & |v| > \delta \\ D[|v+\delta|] + D[|v-\delta|], & |v| \le \delta \end{cases} \qquad \textbf{Equation 4.3 - 3}$$

A plot of both ideal and effective spectral models of Equation 4.2 - 5 and Equation 4.3 - 3 is shown in Figure 4 - 13 for $\alpha = 0.1$, $\beta = 12$ and $\delta = 1/200$. It is apparent that the two curves are totally superposed for the high frequencies, while showing appreciable differences close to dc; near dc the ideal model goes to infinity, while the effective model saturates at the finite value corresponding to its area. This suggests that if the main interest is in the spectral tails, the simpler ideal model of Equation 4.2 - 5 is adequate for the representation of the measured spectrum, and there is no need to represent Equation 4.3 - 2 and Equation 4.3 - 3.

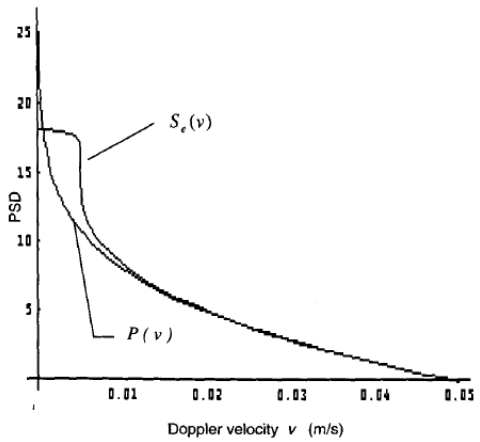

Figure 4 - 13 K-PSD for $\alpha = 0.1$ with and without the effect of finite spectral resolution [Billingsley , 99]

Regarding the FAST measurement in the Montserrat test site, the PSD of the cell located at approximately 260 m (corresponding to the vegetated area) is compared with the simulated K-PSD model in Figure 4 - 14.

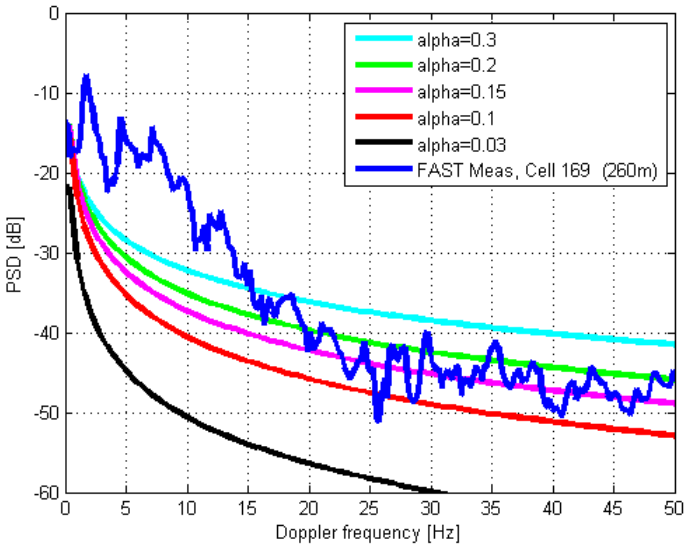

Figure 4 - 14 K-PSD simulation vs PSD of a cell corresponding to a vegetated area (260m) of the FAST measurement

In Figure 4 - 14 can be seen how the cell corresponding to the vegetated area of the FAST measurement in the Montserrat test site fits perfectly the spectral tails of the K-PSD model of Equation 4.2 - 5 for $\alpha = 0.15$. It can also be seen that in the near dc region the model does not matches the measured data which, as expected, saturates at a finite value.

Conclusions

The main objective of this Master Thesis dissertation has been to work with the X Band and the W Band UPC GBSAR sensors to analyze different phenomena that affect to the quality of the focused images in SAR applications.

In chapter 2 the radar imaging basics have been introduced. Radars have been classified between real aperture radars and synthetic aperture radars. The imaging geometry for a radar has been defined, including the azimuth direction, the range direction, the radar swath, the antenna beam pattern on the ground and some radar imaging terms, as the slant range, the ground range or the angles between the sensor and the target.

To enhance signal to noise ratio, chirp modulation is by far the most commonly used modulation because it allows a wide bandwidth while maintaining long pulse duration. It has also been demonstrated that the cross-track resolution in the radar case is independent of the distance between the scene and the radar instrument and is a function of the system bandwidth. The radar equation has been derived and the expression for the signal to noise ratio has been shown.

The differences between real aperture radars and synthetic aperture radars have been exposed. In the real aperture radar case, the resolution in the azimuth direction depends on the length of the antenna as well as the range to the scene. Because of that, such types of radar use the longest antenna possible. On the contrary, in the case of the synthetic aperture radar, the resolution in the azimuth direction is equal to half the length of the physical antenna and it is independent of the range to the scene. In the range domain description, the generation of the signal as a saw-tooth cosine chirp for a continuous wave radar is exposed. It has also been described that the UPC sensor uses the deramping technique at a hardware level for focusing purposes instead of the commonly used matched filter. The deramping process introduces the so called RVP which must be compensated in the processing stage. In this context, the zero-padding technique must be taken into account to easier remove the RVP and to reduce the RCM effect.

For synthetic aperture radars, the back projection focusing algorithm has been analyzed, as well as the cross range sampling conditions. Finally, the slant range distortions of foreshortening, layover and shadowing that affect the focused image have been exposed.

In chapter 3, the influence of an oscillating target in a GBSAR focused image has been analyzed. With this purpose, two different systems of the UPC laboratory have been used: the X band GBSAR operating at a frequency of 9.65GHz and the W band GBSAR operating at a frequency of 94GHz. It has been observed that an oscillating target in the cross-range direction does not affect to the focused image. On the contrary, it has been demonstrated that an oscillating target in the range direction does not appear as a static target in the focused image. Specifically, the oscillating target in the range direction tends to be expanded in the cross range direction, which means a spreading of its cross range spectrum. But if the oscillation of the target is too fast with respect to the sampling frequency, the result is the apparition of some replicas in the same radial range. This effect has been observed in some measurements with the X band GBSAR in a crane oscillating approximately 20mm at a distance of roughly 500m and with the W band GBSAR and a speaker oscillating nearly 0.5mm at a distance of 5.6m.

In chapter 4, a model for the Doppler spectrum of windblown radar ground clutter has been presented. An expression for the K-PSD model, which matches perfectly the exponential shape of the ac region in the measured spectrum for vegetated areas, has been derived.

With the X-band UPC GBSAR, some experiments in the Collserola test site and in the Montserrat test site have been performed to observe the effect of the scintillation of the vegetation in the focused images. It has been evidenced the relation between the wind speed, the scintillation of the vegetation and the blurring effect that appears in the cross range direction in the final image. The validity of the K-PSD model has been demonstrated by comparing the theoretical curves with the measured PSD.

By means of working with two different acquisition modes with the X-band UPC GBSAR (STOP & GO and FAST), the relation between the observation time and the increase of the blurring effect has been demonstrated.

Regarding to the W band sensor, the sensibility of the system to atmospheric conditions, such as the temperature, has been evidenced. After the stabilization time inherent of the system, fluctuations of the temperature can introduce qualitative errors in the measured phase. It has been also demonstrated that range displacements of 5 μm in the range direction are resoluble by the W band UPC radar.

Appendix A

Ap.1 Introduction

The polarimetric X Band GBSAR used for the acquisitions exposed in the present Master Thesis dissertation has been developed by the RSLab at the UPC. Said sensor is an evolution of the GBSAR, also developed by the RSLab, based on the *Direct Digital Synthetizer* (DDS) [Aguasca, 04]. It is important to describe the main architecture of the sensor as well as its performance characteristics since all the measurements presented in this dissertation have been done with the UPC system.

In the new model of X Band GBSAR, the most important change has been done in the manner in which the sensor generates the signal to be transmitted. Concretely, the DDS has been substituted by a *Phase-Locked Loop* (PLL), as will be analyzed in the present section.

Ap.2 Comparing the architecture of the DDS-based and the PLL-based UPC X-Band GBSAR sensors

The GBSAR sensor essentially consists of a CW radar system mounted on a sliding support that synthesizes in time an aperture longer than the physical dimension of the transmitting and receiving antennas. The radio-frequency block consists of three main parts:

- Generation of the signal.
- Radar front-end, which performs the transmission and reception of the signal.
- Raw data demodulation, sampling and storing.

The synthetic aperture is carried out through the movement of the front-end along a linear rail controlled via computer. This basic structure is resumed in Figure Ap - 1.

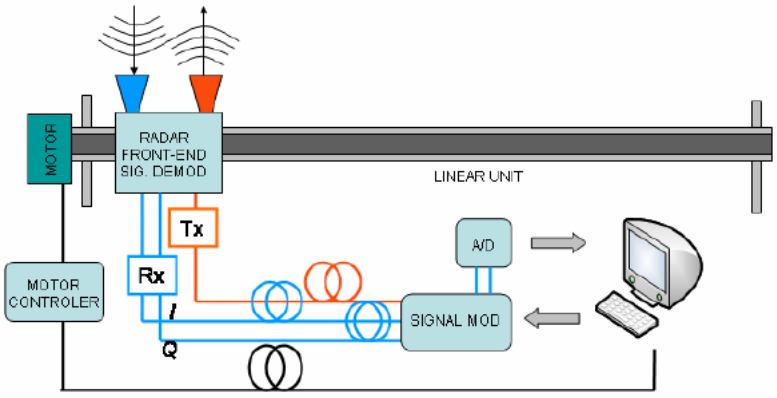

Figure Ap - 1 Blocks-Scheme of the (DDS-based) UPC X Band GBSAR sensor

The GBSAR sensor based on the DDS was developed to optimize the signal generation and transmission in order to obtain a high quality CW-FM signal and to reduce the time required for the scanning process. The PLL-based sensor maintains the same philosophy but overcoming some limitations when using the DDS, together with a improvement of the performance of the system. Both radar architectures are based on FM-CW modulated solid-state transmitter designed to be flexible and adaptable to different frequency bands, such as L-, C-, X-, and Ku-bands. The first improvement of the PLL-based sensor resides in the flexibility and adaptability of the system to different signal bandwidths and frequency bands. In the DDS-based sensor, the system is modular and the change of frequency band can be only done by interchanging the frequency multiplication module. This is a tedious task that in practice is translated in the necessity of constantly modify the signal generation board at hardware level. Aversely, the PLL-based system has the capability to change the operation frequency by simply changing the *Voltage Controlled Oscillator* (VCO) chip and by properly programming the registers of the PLL chipset at software level. In addition to that, the system is prepared to be easily accessible to the programming of the PLL through an USB port, as will be explained later.

The schematic description of the DDS-based GBSAR is shown in Figure Ap - 2.

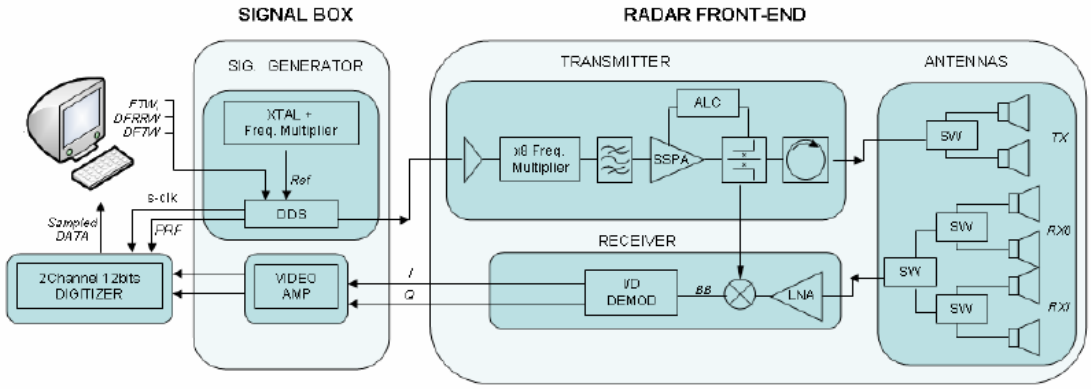

Figure Ap - 2 Internal architecture of the (DDS-based) UPC X Band GBSAR system

In this case, the frequency generation module is based on a Direct Digital Synthesis (DDS) chipset [Analog]. This device is a programmable high speed D/A converter capable to synthesize analog sine-waves by fast frequency hops and a very fine tune resolution. Its versatility makes it possible to digitally generate analogical and digital modulated signals by loading the configuration parameters into its internal registers. For GBSAR applications, the DDS is set up to generate chirp modulated signals. An external clock is used as reference to increment output signal frequency without generating phase discontinuities. The output is an L-Band FM-modulated signal that must be bandpass-filtered to eliminate spurious replicas generated by the D/A conversion. A final x8 frequency multiplier provides a chirp centered at 9.65 GHz.

The schematic description of the PLL-based GBSAR is shown in Figure Ap - 3.

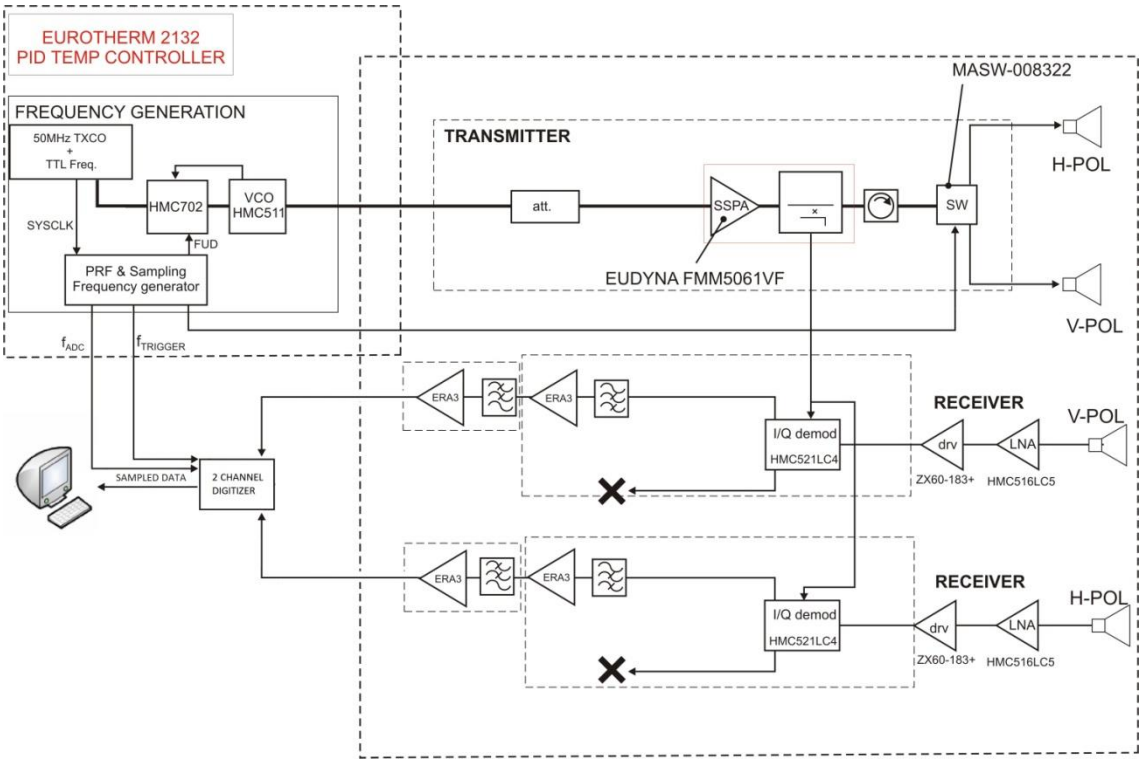

Figure Ap - 3 Internal architecture of the (PLL-based) UPC X Band GBSAR system

The most important difference between the schematic description of Figure Ap - 3 and Figure Ap - 2 is the signal generation. In the schematic of Figure Ap - 3, the signal generation is based in a PLL and a VCO chipsets [Hittite]. The PLL chipset (HMC702LP6CE) is a SiGe BiCMOS fractional-N frequency synthesizer. The fractional synthesizer features an advanced delta-sigma modulator design that allows ultra-fine frequency step sizes. The synthesizer features the ability to alter both the phase-frequency detector (PFD) gain and the cycle slipping characteristics of the PFD. This feature can reduce the time to arrive at the new frequency by 50% vs. conventional PFDs. Ultra low in-close phase noise also allows wider loop bandwidths for faster frequency hopping. The synthesizer contains a built-in linear sweeper function, which allows it to perform frequency chirps with a wide variety of sweep times, polarities and dwells, all with an external or automatic sweep trigger. The VCO (HMC511LP5) is a GaAs InGaP Heterojunction Bipolar Transistor (HBT) MMIC VCO. The VCO's phase noise performance is excellent over temperature, shock, and process due to the oscillator's monolithic structure. The PLL-based signal generation board used in the X Band GBSAR can be seen in Figure Ap - 4.

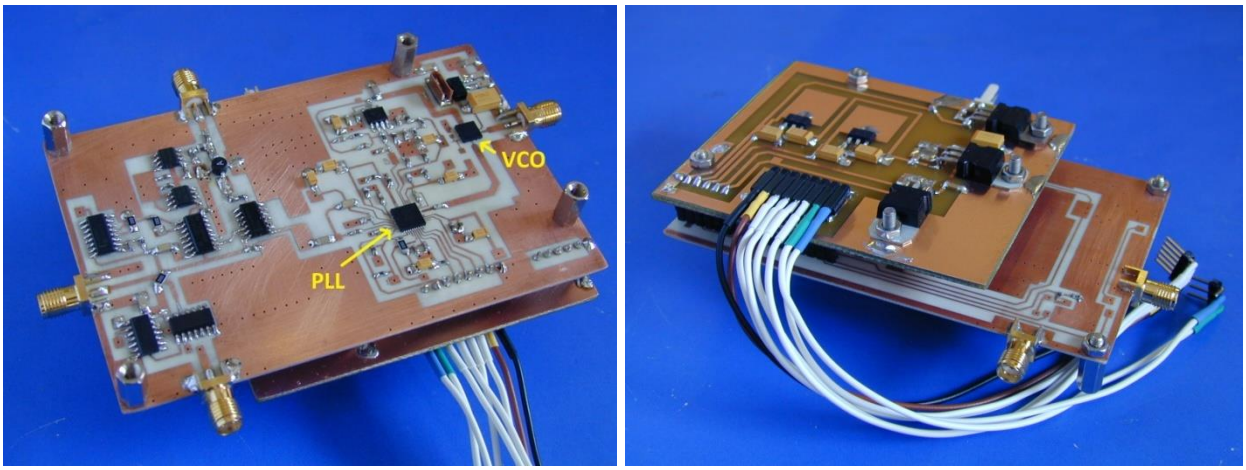

Figure Ap - 4 PLL-based signal generation board. Left: Bottom side of the board. Right: Top side of the board

The signal generation board of Figure Ap - 4 contains a 50 MHz oscillator used as a reference, the PLL chipset (HMC702LP6CE), the VCO (HMC511LP5) chipset, an operational amplifier, the loop filter of 60 KHz, some voltage regulators and a connector used to communicate the PLL chipset with a microcontroller. One of the functions of the microcontroller integrated in the SAR system is to programming the registers of the PLL. The microcontroller, accessible through a USB port, makes easy the task of modifying the parameters of the PLL.

Ap.3 PLL-based UPC X-Band GBSAR signal generation block analysis

Figure Ap - 5 shows the signal generation block integrated in the SAR system.

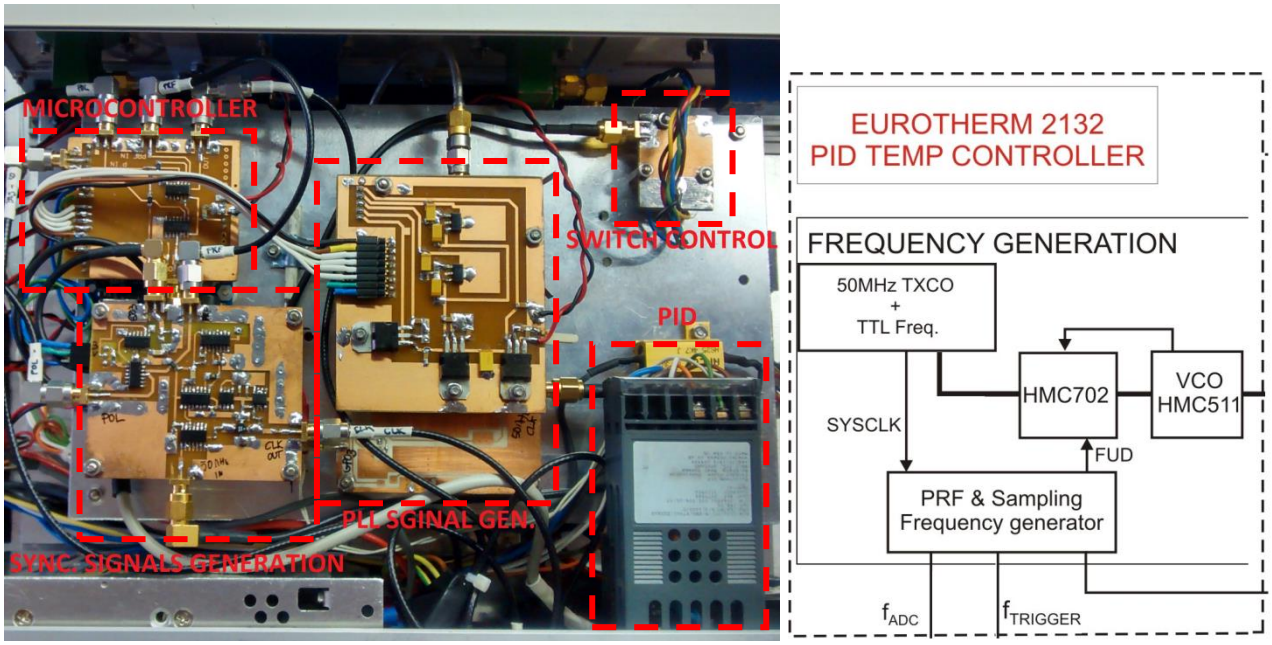

Figure Ap - 5 Signal generation block integrated in the system

The different elements composing the signal generation block in Figure Ap - 5 are the signal generation board shown in Figure Ap - 4, the PID temperature controller, a board responsible

of generating all the synchronous signals, the microcontroller and a board responsible of controlling the high frequency solid state switch.

The PID temperature controller is responsible of maintaining the system at a fixed temperature. The board responsible of the synchronous signals generation takes the 50 MHz reference from the PLL signal generation board and generates the Pulse Repetition Frequency (PRF) used to digitalize the signal, a signal called POL to control the switch and a signal called GPO3 used to properly programming the PLL. As the PLL generates a triangular cosine chirp, the function of the GPO3 signal is to set the start of the up ramp and the down ramp. The microcontroller programs the PLL and also is responsible to control all the signals mentioned before to properly work in the different modes of operation of the SAR. Finally, the switch control board takes the POL signal and uses it to control the switch between its two outputs, allowing the system to transmit in vertical or horizontal polarization.

Once the signal is generated by the PLL signal generation board, the last step before transmitting it is the Power Amplification. At this point of the circuit, a sample of the transmitted signal is extracted by a directional coupler and injected to the receiver block for the deramping process.

Ap.3.1 PLL signal generation and loop filter

The PLL chipset generates the frequency ramp to generate the chirp signal by means of a set of N dividers. Said dividers generate undesired spurious that can affect the system performance if the loop filter is not properly designed [Hittite]. Figure Ap – 6 shows the focused image of an acquisition over an equivalent empty scenario.

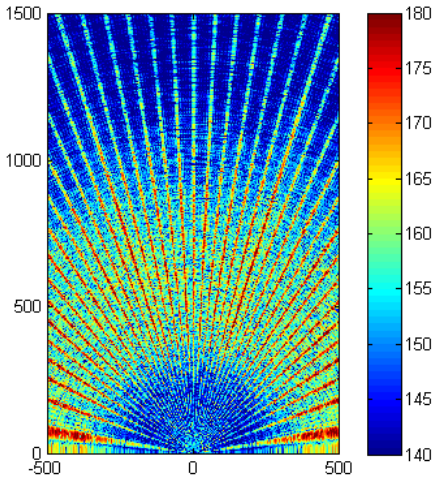

Figure Ap - 6 Undesired spurious in the focused image

The vertical lines across the image in Figure Ap – 6 are undesired spurious coherent with the reference signal that are not suppressed by the loop filter. If the loop filter is not properly designed, such spurious will be present in the final image degrading its quality and masking useful information. In the image, the effect of the low-pass and high-pass filters of the receiver chain, which will be characterized in the following section, can also be observable. Such effect can be seen in the background noise, which has less intensity for low frequencies and for high

frequencies, corresponding with the cut-off frequency of the filters. Figure Ap – 7 shows the filter designed for the PLL-based UPC X Band sensor and all the noise contributions of the PLL.

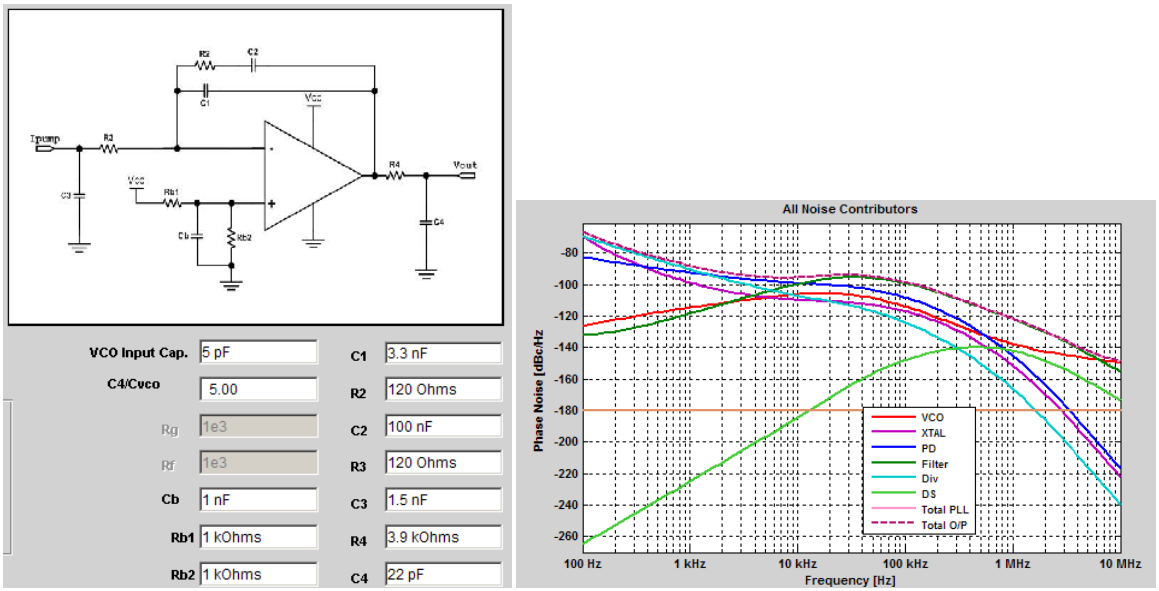

Figure Ap - 7 Left: Loop filter with bandwidth of 60 KHz. Right: All noise contributions of the PLL

The filter of Figure Ap – 7 left is the active C filter of fourth order used in the final design. The RC components in the output of the operational amplifier are extremely important because they are in charge of suppressing of the spurious showed in Figure Ap – 6. Figure Ap – 7 right shows the whole noise contributions of the PLL. The light blue line shows the contribution of the noise introduced by the dividers and filtered by the selected loop filter. The final loop components have been chosen not only taken into account the PLL loop response but mitigating the effect of the noise from the internal dividers. Empirically the equivalent loop filter bandwidth has been selected to 60KHz that is a trade-off between loop response, equivalent PRF of the system and noise mitigation.

Ap.3.2 Commutation between transmission antennas

Another hardware improvement included in the new GBSAR system is the use of solid state switches in the transmitting antennas, as it is another distinctive element with respect to the DDS-based sensor. The component employed to switch between the two transmission antennas is the MASW-008322 from Macom [Macom]. It is a GaAs Single Pole Double Throw (SPDT) with high isolation and very broadband performance. Figure Ap - 8 shows the functional schematic of the switch and implemented board for it.

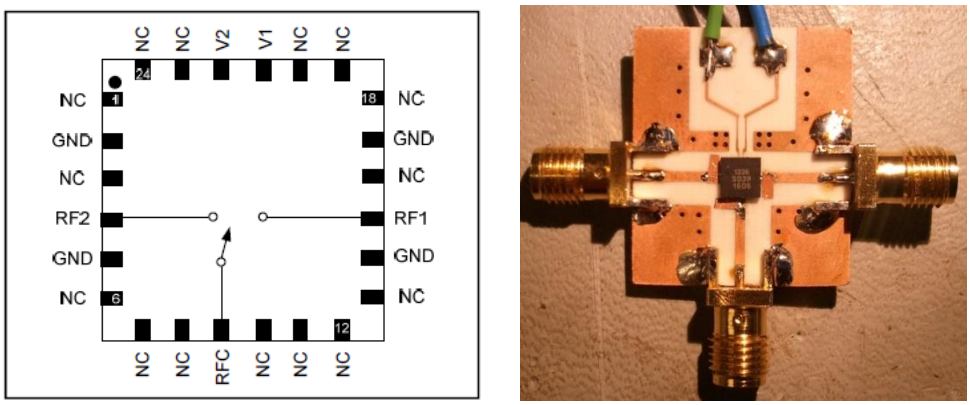

Figure Ap - 8 Left: MASW-008322 functional schematic. Right: Board implemented for the MASW-008322

The measured insertion losses, return losses and isolation of the board of Figure Ap - 8 are shown in Figure Ap - 9. The switch has an input and two outputs called RF1 and RF2.

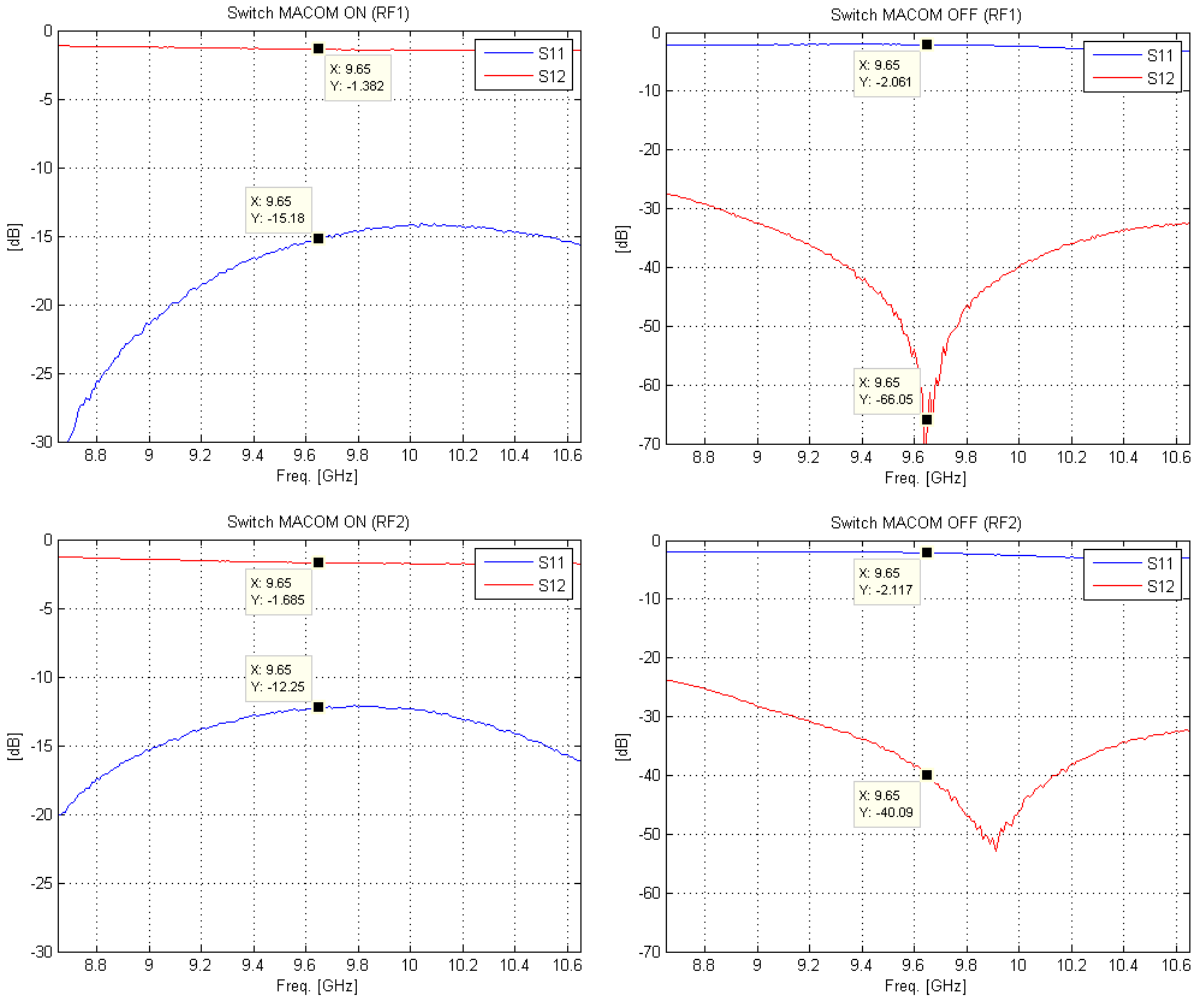

Figure Ap - 9 Top Left: Insertion losses and return losses in RF1. Top Right: Isolation in RF1. Bottom Left: Insertion losses and return losses in RF2. Bottom Right: Isolation in RF2.

As can be seen in figure Figure Ap - 9, for the RF1 port the return losses are -15.2 dB, the insertion losses -1.3 dB and the isolation between RF1 and RF2 is -66 dB at the desired frequency of 9.65 GHz. On the other hand, when in the port RF2 the return losses are -12.2 dB,

the insertion losses are -1.6 dB and the isolation between the two ports is -40 dB. The two ports are not symmetric but in both cases the response is acceptable.

The truth table of the switch is shown in Figure Ap - 10.

Control Inputs		Condition of Switch	
V1	V2	RF1	RF2
High	Low	Off	On
Low	High	On	Off

Figure Ap - 10 Truth table of MASW-008322. Vlow= -5V. Vhigh=0V

To generate the control inputs V1 and V2, the board shown in Figure Ap - 11 has been implemented.

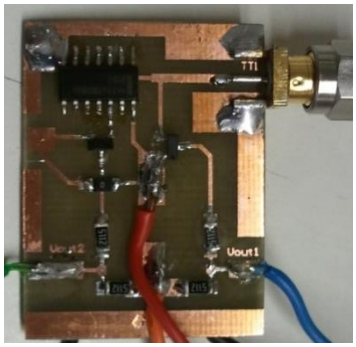

Figure Ap - 11 Board responsible to control the switch commutation

The board of Figure Ap - 11 consists of two channel P transistors which are responsible to generate the different states of V1 and V2 that compound the truth table. The signal POL generated from the synchronous generation signals board is introduced to the switch control board. POL is a rectangular wave of half the frequency of the PRF, which ensures that for every triangular wave of the chirp signal the switch has commutated. Figure Ap - 12 shows the measured V1 and V2 control inputs.

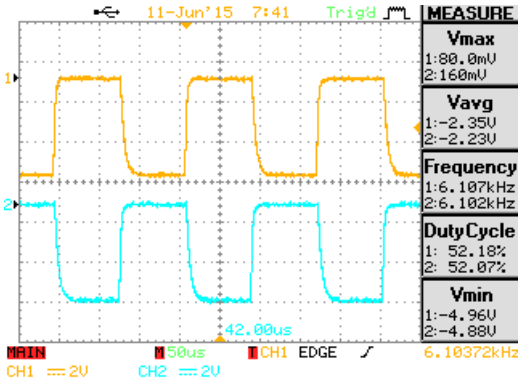

Figure Ap - 12 Measured V1 and V2 control inputs

It is obvious in Figure Ap - 12 that when one of the signals has 0 V the other has -5V and vice versa. It can be seen that there exist a rise and a fall transient time due to the transistors. Figure Ap - 13 shows the measured transient time.

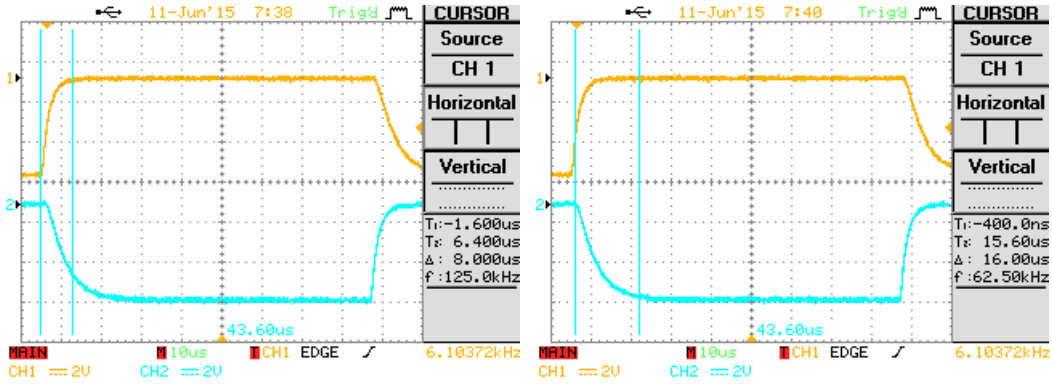

Figure Ap - 13 Left: Measured rise time of control input. Right: Measured fall time of control input

In Figure Ap - 13 can be observed that the rise time is 8 µs and the fall time 16 µs, which is sufficiently fast to does not affect the performance of the system.

To validate the proper behavior of the switch and its synchronism with the PRF, a new measurement is realized. The switch is integrated just before the transmitting antennas such that the transmitted signal will switch between vertical and horizontal polarization. In reception, just the horizontal polarization is measured. Figure Ap - 14 shows a measurement with the oscilloscope of the received signal superposed to the PRF.

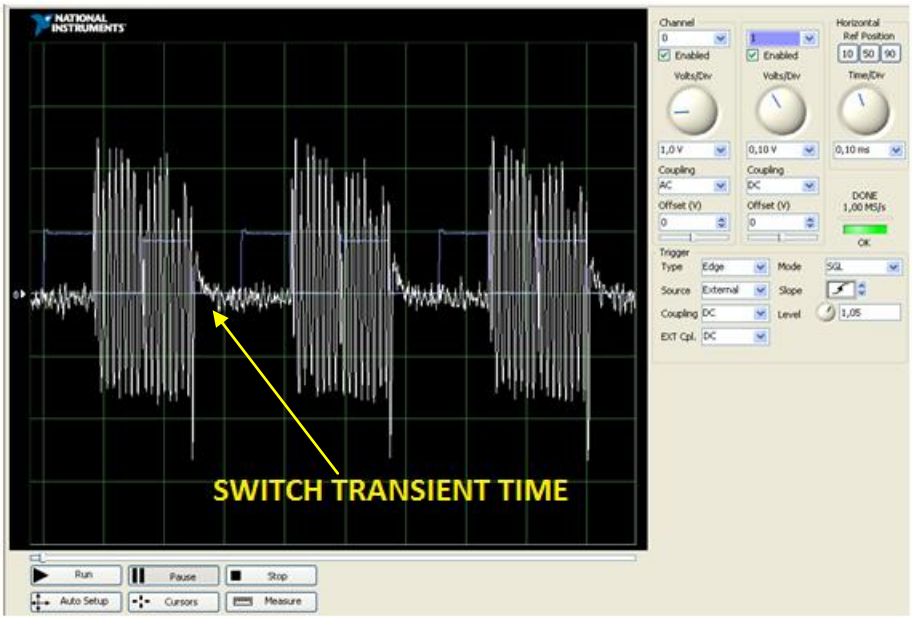

Figure Ap - 14 Oscilloscope measurement. Channel 0: received signal in horizontal polarization. Channel 1: PRF

The digitizer uses the rising edge of the PRF to acquire the received data. Figure Ap - 14 shows that for the first rising edge of the PRF (channel 1) the received signal (channel 0) has no signal and that for the second rising edge the received signal has signal and so on. Assuming that when the transmitting polarization is vertical the reception in the horizontal polarization must be almost zero, the system is working properly. After a careful observation of the received signal in channel 0, the falling transient time of the switch can be seen. As the digitizer uses the rising edge of the PRF to acquire the signal, the last samples stored coincident with the falling

transient time can be affected. Is not the case of the rising transient time, which is not coincident with any acquisition interval.

Ap.4 PLL-based UPC X-Band GBSAR receiver front-end

The transmission and reception of the microwave signal is carried out by the front end module showed in Figure Ap - 15.

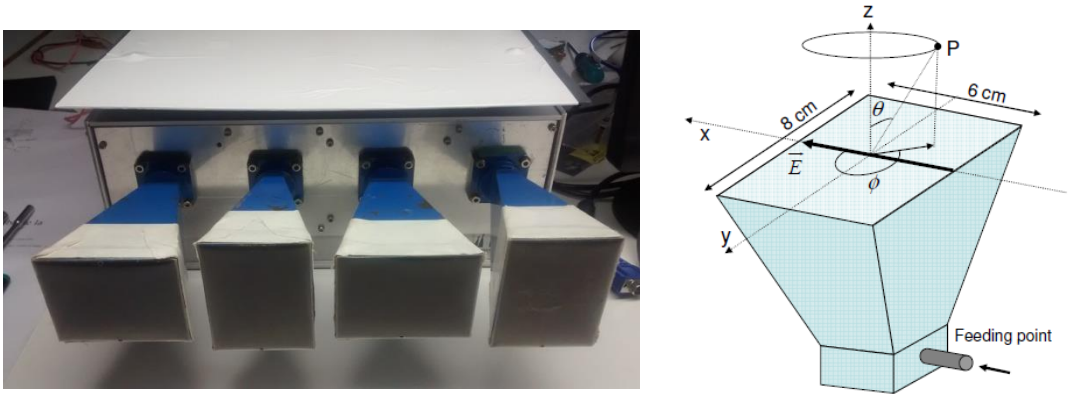

Figure Ap - 15 Left: Front end of the PLL-basedUPC X Band GBSAR. Right: Sketch of the X Band horn antenna mounted on the front-end.

In order to provide full polarimetric (PolSAR) measurements, four identical linearly-polarized pyramidal horns are installed on the radar front-end (Figure Ap - 15 right). The two antennas on the left are the transmission ones, with vertical and horizontal polarization respectively. The antennas in reception are the ones on the right side of the image, also with vertical and horizontal polarization. Full polarimetric data is acquired by switching the transmission antennas and storing the data from the two reception channels simultaneously as showed in Figure Ap - 16.

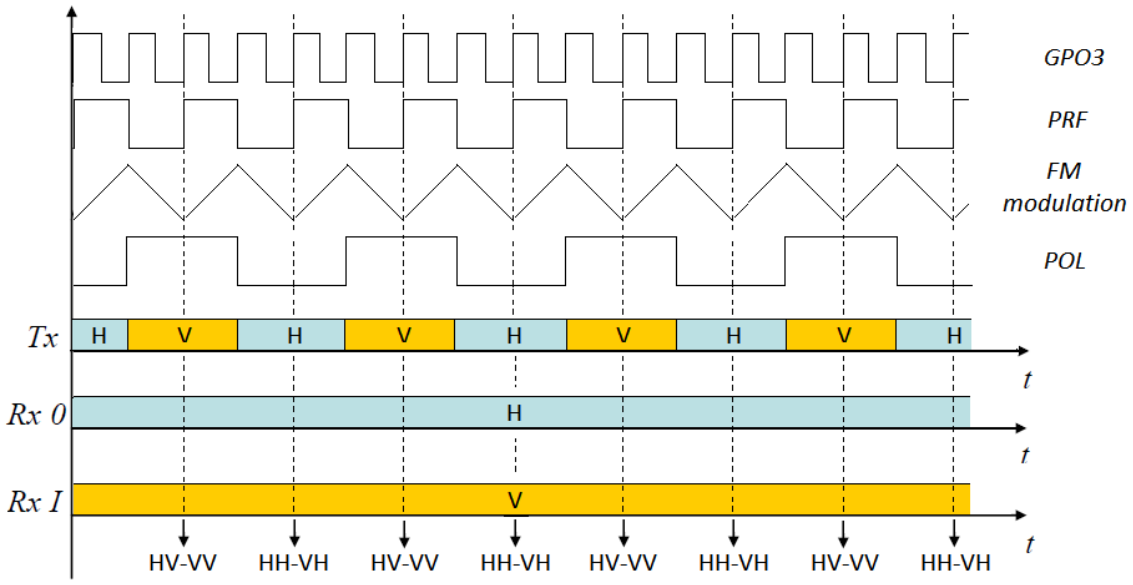

Figure Ap - 16 Diagram of the PLL-based UPC GBSAR to gather PolSAR miasurements. Tx denotes the transmitting antenna, Rx 0 is the reception channel 0, Rx 1 is the reception channel 1, H denotes Horizontal and V vertical

Figure Ap - 16 shows the signals generated by the synchronous signal generation board. As can be seen, the signal GPO3 sets the start of the ascendance and the falling of the FM modulation. The POL signal sets the commutation of the switch and the rising edge of the PRF sets the start of the acquisition to the digitizer. The digitizer employed has two acquisition channels to store the data simultaneously. This way, following the diagram of Figure Ap - 16, when the polarization in transmission is vertical the digitizer acquires the polarization HV in channel 0 and VV in channel 1. Coherently, when the transmitted polarization is horizontal, the channel 0 acquires the HH polarization and channel 1 the VH.

In Figure Ap - 3 can be appreciated that the first element in the reception chain after the receiving antenna is a Low Noise Amplifier (LNA). Regarding to the Friis' formula showed in Equation Ap - 1, the overall noise figure of the receiver's front-end is dominated by the first stage.

$$F_{total} = F_1 + \frac{F_2 - 1}{G_1} + \frac{F_3 - 1}{G_1 G_2} + \frac{F_n - 1}{G_1 G_2 \dots G_{n-1}} \qquad \textbf{Equation Ap - 1}$$

Using an LNA, the effect of noise of from subsequent stages of the receive chain is reduced by the gain of the LNA. In addition to the LNA, three more amplifiers are located at different points of the receiving chain. One after the LNA, another after the high-pass filter and the last one after the low-pass filter. The total gain of every receiving chain is around 73 dB.

After the second amplifier there is a compact I/Q MMIC mixer (HMC521LC4) [Hitite], which performs the down-conversion frequency to the Intermediate Frequency (IF). The high-pass RC filter of the receiving chain, whose cutoff frequency is 12 MHz, aims to penalize very close targets with high reflectivity. On the other hand, the low-pass RC filter, whose cutoff frequency is 25 MHz, aims at eliminating undesired signals. Figure Ap - 17 shows the response of both filters.

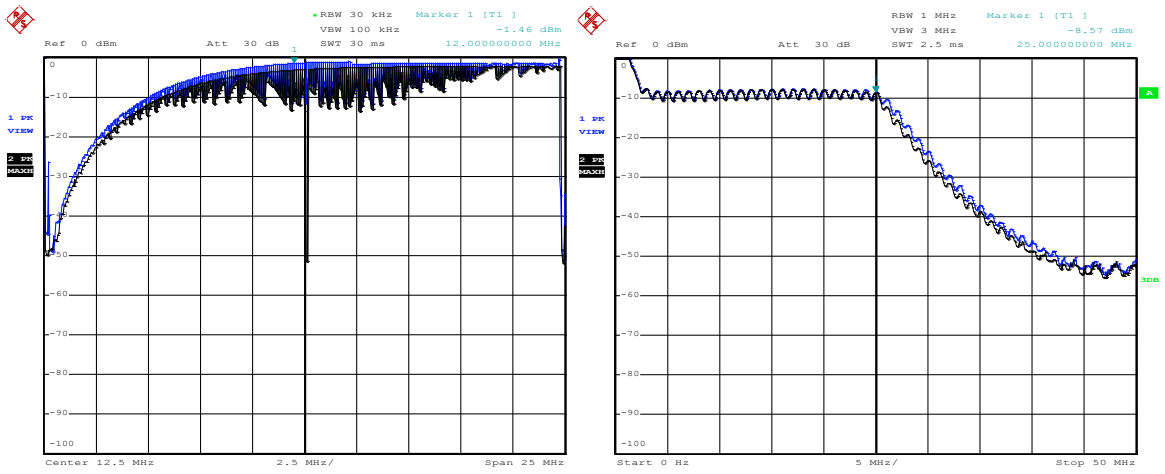

Figure Ap - 17 Left: Response of the high-pass filter with cutoff freq. at 12 MHz. Right: Response of the low-pass filter with cutoff freq. at 25 MHz.

The last step of the receiving channel is the sampling and storing of the received signal. As mentioned before, this is done by a two channel digitizer. The digitizer uses the PRF as a rise edge trigger to start the acquisition and the reference if 50 MHz as a frequency sampling rate.

Ap.5 Operation modes of the PLL-based UPC X-Band GBSAR

Another function of the microcontroller integrated in the system is to proportionate the flexibility to work in different operation modes. The operation modes are:

- FAST V POL: transmitting in vertical polarization and receiving in both polarizations while realizing a measurement in the FAST mode.
- FAST H POL: transmitting in horizontal polarization and receiving in both polarizations while realizing a measurement in the FAST mode.
- FAST FULL POL: transmitting and receiving in both polarizations while realizing a measurement in the FAST mode.
- STOP & GO V POL: transmitting in vertical polarization and receiving in both polarizations while realizing a measurement in the STOP & GO mode.
- STOP & GO H POL: transmitting in horizontal polarization and receiving in both polarizations while realizing a measurement in the STOP & GO mode.

In the STOP & GO mode, a full polarimetric measurement can also be done by interchanging the transmitting polarization in every position of the antenna along the linear unit.

Ap.6 DDS-based vs PLL-based UPC X-Band GBSAR focused Images

The main advantages of the PLL with respect to the DDS are its ultra low phase noise, its capability to obtain the desired frequency and its versatility to control sweep times when performing the frequency chirp. This better performance has its impact in the final focused image. Figure Ap - 18 shows a full polarimetric measurement realized in the Collserola test site using the PLL-Based UPC X Band GBSAR operating in FAST mode.

Figure Ap - 18 shows good background noise due to the good stability in phase of the PLL. After analyzing the focused images, it can be concluded that the UPC PLL-based sensor constitutes a reliable prototype of a new generation of fast GBSAR systems that make it possible to acquire high-quality zero-baseline PolSAR data without any revisit time constraint.

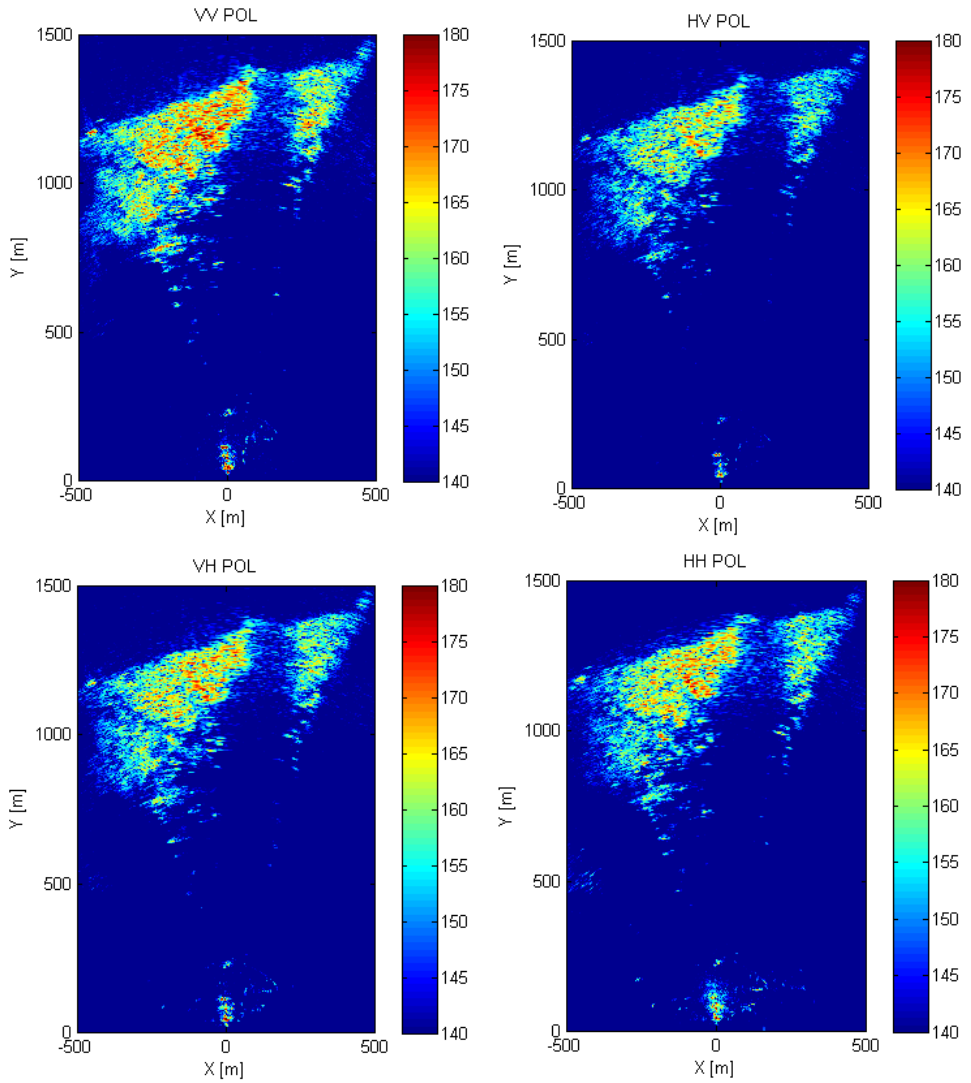

Figure Ap - 18 Measurement in the Collserola test site with the UPC PLL-Based X Band GBSAR operating in FAST mode. Top Left: VV POL. Top right: HV POL. Bottom left: VH POL. Bottom right: HH POL.

Bibliography

[Aguasca , 04] A. Aguasca, A. Broquetas, J. Mallorqui, and X. Fàbregas, "A Solid State L to X-band Flexible Ground-based SAR System for Continuous Monitoring Applications", *Proceedings of IGRS IEEE Symposium Igarss'04*, Anchorage, USA, September 2004.

[Analog] Direct Digital Synthesizer AD9858 Data-sheet, available online at http://www.analog.com/UploadedFiles/Data_Sheets/AD9858.pdf.

[Billingsley , 87] Billingsley, J.F. Lanabee, *"Measured spectral extent of Land X-band radar reflections from wind-blown trees"*, MITLincolnLaboratory, Project Report CMT-58, February 1987.

[Billingsley , 96] Billingsley, *"Exponential decay in windblown radar ground clutter Doppler spectra: multifrequency measurements and model"*, MIT- Lincoln Laboratory, TR-997, July 1996.

[Billingsley , 99] Billinglsey, "*A New Model for the Doppler Spectrum of Windblown Radar Ground Clutter*", The record of the 1999 IEEE Radar Conference, Waltham, 20-22 April 1999.

[Billingsley , 02] Billinglsey, "*Low-Angle Radar Land Clutter*", Norwich, NY 13815, 2002, ISBN 1-891121-16-2.

[Curlander, 91] J.C. Curlander and R.N. McDonough, *Synthetic aperture radar: systems and signal processing*, New Cork, Wiley, 1991.

[Hittite] Phase Locked Loop HMC702LP6CE Data-sheet, Voltage Controlled Oscillator HMC511LP5 Data-sheet and HMC521LC4 Data-sheet available online at https://www.hittite.com/.

[Ishimaru, 78] A. IIshimaru*, Wave Propagation and Scattering in Random Media, Single Scattering andTransport Theory (Vol. 1)*, Academic Press Inc., California, USA, 1978.

[Zyl, 10] J. Van Zyl, Yujin Kim, *Synthetic Aperture Radar Polarimetry*, Jet Propulsion Laboratory California Institute of Technology, December 2010.

[Levanon,04] N. Levanon and E. Mozeson*, Radar Signal*, John Wiley & Sons, Inc., Hoboken, NewJersey, 2004.

[Hittite] Switch MASW-008322 Data-sheet available online at http://cdn.macom.com/datasheets/MASW-008322.pdf.

[Pipia, 09] L. Pipia, X. Frabegas, *"Polarimetirc Diferential Sar Interferometry with Ground-Based Sensors"*, Barcelona, July 2009.

[Proakis, 98] J. G. Proakis and D.G. Manolakis, *Tratamiento Digital de Señales 3a ed.*, PearsonEducation S.A., Madrid, 1998.

[Skolnik, 90] M. Skolnik*, Radar Handbook*, Mc Graw-Hill. 1990.

[Soumek, 99] M. Soumekh, *Synthetic Aperture Radar Signal Processing*, John Wiley & Sons Inc., NewYork, 1999.

[Yegulalp, 99] A.F. Yegulalp, *"Fast Backprojection Algorithm for Synthetic Aperture Radar"*, The record of the 1999 IEEE Radar Conference, Waltham, 20-22 April 1999.